

NANOWIRE-BASED BETAVOLTAIC
GENERATORS

SIMULATION AND OPTIMIZATION OF NANOWIRE-BASED
BETAVOLTAIC GENERATORS

BY

DEVAN L. WAGNER, B.Eng.Mgt

A THESIS

SUBMITTED TO THE DEPARTMENT OF ENGINEERING PHYSICS

AND THE SCHOOL OF GRADUATE STUDIES

OF MCMASTER UNIVERSITY

IN PARTIAL FULFILMENT OF THE REQUIREMENTS

FOR THE DEGREE OF

MASTER OF APPLIED SCIENCE

© Copyright by Devan L. Wagner, June 2020

All Rights Reserved

Master of Applied Science (2020)
(Engineering Physics)

McMaster University
Hamilton, Ontario, Canada

TITLE: Simulation and Optimization of Nanowire-Based
Betavoltaic Generators

AUTHOR: Devan L. Wagner
B.Eng.Mgt, (Engineering Physics and Management)
McMaster University, Hamilton, Canada

SUPERVISORS: Dr. Ray R. LaPierre
Dr. Dave R. Novog

NUMBER OF PAGES: xv, 109

Lay Abstract

Widely used batteries, such as lithium-polymer cells, are bulky and suffer from short discharge times or temperature sensitivity. Betavoltaics – also known as “nuclear batteries” – offer an opportunity to surpass these issues.

Beta particles, or energetic electrons, are the result of certain nuclear decay reactions. Betavoltaic batteries create electricity from these particles, can remain active for hundreds of years, and are insensitive to environmental conditions. In addition, these particles are easy to shield, rendering them safe for users.

This work focuses on a new type of betavoltaic which uses nanowires to capture more beta particles and ultimately improve performance. These devices have been designed through a simulation-based approach that has maximized the total power output as well as efficiency by fine-tuning different parameters. The designs described in this work exhibit huge improvements over conventional devices and will allow nanowire-based betavoltaics to compete with the top performing devices developed to date.

Abstract

In order to increase the efficiency of betavoltaic devices, an architecture utilizing nanowires has been developed. In this architecture, a radioisotope is deposited between a nanowire array in order to increase the fraction of β particles captured by the semiconductor converter and minimize the energy lost to self-shielding. Previous work has prototyped such a design; however, performance was limited to an efficiency of 0.5%. This thesis outlines the design and optimization of the nanowire-based betavoltaic generator. Both the nanowire array geometry and the nanowire p-i-n diode design are optimized for maximum radiation capture and conversion efficiency, respectively.

First, a model was developed in the GEANT4 Monte Carlo toolkit in order to investigate the radiation capture of various array geometries. Radioisotope sources of elemental ^3H , ^{63}Ni , and ^{147}Pm , as well as compounds of each were examined with gallium phosphide nanowires. Overall, it was found that nanowires should be grown as long as possible to accommodate the most source material while the ratio of the diameter to array pitch can be optimized for maximum power capture. Optimized arrays presented an improvement in energy capture of approximately 6 and 15 times for ^{63}Ni and ^3H devices, respectively, while ^{147}Pm devices indicated no improvement. Optimized array geometry was extended to both silicon and gallium arsenide and the

radiation capture simulations were coupled to drift-diffusion calculations in COMSOL Multiphysics for axial junction nanowires. Following the junction optimization, devices were predicted to be between 4 and 10% efficient with power outputs ranging from 2 to 6 $\mu\text{W cm}^{-2}$. Despite the large improvement compared to experimental results, surface recombination was found to limit the performance of long gallium phosphide nanowires. Therefore, core-shell junctions were then investigated and found to improve upon all axial designs.

Overall, it has been determined that the nanowire device design is advantageous over planar betavoltaics due to the mitigation of self-shielding effects. Devices utilizing 10 μm long gallium phosphide core-shell nanowires with a ^3H source are predicted to achieve the top performance of 12% efficiency and a power density of 7 $\mu\text{W cm}^{-2}$. In addition, gallium phosphide and gallium arsenide devices with ^{63}Ni are able to achieve an energy density in excess of 1 Wh cm^{-2} due to the long half-life.

To my parents, grandparents, and sisters

I'm only here today because you taught me the importance of curiosity

Acknowledgements

First and foremost, I'd like to thank both of my supervisors, Dr. Ray LaPierre and Dr. Dave Novog, for their support – both academic and otherwise – throughout my thesis. Each of you have offered invaluable insight into my work, pushed me to learn more than what is necessary, and have advocated for my success every step of the way. Thank you for sharing your experiences with me both in our group meetings (that always seemed to go too long) and over beers at The Phoenix (which seemed to never last quite long enough).

In addition to supervision, both the LaPierre and Novog research groups have provided me with incredible colleagues along the way. Special thanks to Simon McNamee, Paige Wilson, and Ara Ghukasyan for getting me started with the project, spit-balling ideas, and showing me how to use COMSOL without relying too much on forum posts. Also, thanks to each of my office mates in ETB: each of you have always made Mondays more tolerable and I am grateful to have shared my day-to-day with all of you.

Beyond my academics, there are several communities that I am a part of and that I owe a great deal of thanks. The Eng Phys department has also always been a strong community and something I have enjoyed about my time at McMaster for seven (!) years now. Although there are far too many people to thank individually,

I'd like to give a special thank you to Peter Jonasson and Dr. Harold Haugen. It has always been a pleasure running into both of you around campus; thank you for your uncanny ability to brighten people's day. I'd also be remiss not to mention McMaster NEUDOSE. I had no idea when I signed up in 2015 that the team would become such an important aspect of my life. I owe a huge gratitude to each member of the team (past and present) for helping me find passion outside of work and establishing a group of people that I hope to see succeed long after our satellite ceases operation. Thank you for everything you've taught me and for being so good at what you do that you've made my job so easy in recent times.

A very special thank you goes out to my friends and family as well. To my friends: whether we are playing D&D, Magic, watching the latest installment of Star Wars, or making fun of the latest installment of Star Wars, thank you for sharing your time and giving me something to always look forward to. To my family: thank you for your unending support and indulging me when I want to talk about nuclear batteries, space, or anything nerdy. Holidays and visits with each other may never last long enough but they've always been invaluable to me, especially during my Masters. Specifically to Charlotte, I can't wait to meet you and for all the things we can teach each other.

Last, and definitely not least, I'd like thank my partner and love of my life, Taylor Stimpson. Thank you for going through this journey alongside me and for your unwavering support. I could write an entire thesis-worth of material thanking you but, in short, I am proud of both of us and can't wait for what comes next.

Contents

Lay Abstract	iii
Abstract	iv
Acknowledgements	vii
Notation & Abbreviations	xiv
Preface & Declaration of Academic Achievement	xv
1 Introduction	1
1.1 Background	1
1.2 Literature Review	4
1.3 Motivation	5
1.4 Goal & Outline of Thesis	6
2 Optimization of Energy Capture	10
2.1 Introduction	12
2.2 Modeling Energy Capture	16
2.3 Nanowire Geometry Optimization	19

2.4	Conclusions	24
3	Coupled Simulation for Total Power Optimization	29
3.1	Introduction	31
3.2	Monte Carlo Simulations and Array Geometry Optimization	36
3.3	Charge Transport Modeling	42
3.4	Optimized Device Performance	47
3.5	Conclusions	50
4	Core-shell Structures	58
4.1	Introduction	60
4.2	Methods	63
4.3	Results & Discussion	66
4.4	Conclusion	72
5	Discussion & Conclusion	77
5.1	Summary & Discussion	77
5.2	Future Work	79
5.3	Conclusion	80
A	Supporting Information for Ch. 3	83
B	Supporting Information for Ch. 4	102

List of Tables

1.1	Commercially available betavoltaic devices	5
2.1	Validation of β -generated current calculations	18
2.2	Optimized β -generated current	23
3.1	Device performance comparison	49
4.1	Best-case energy capture for infinitely-long nanowires	63
4.2	Comparison of optimum device efficiencies	71
5.1	Top device performance	78
A.1	Variables used in radiation interaction simulations.	84
A.2	Integrated captured power in nanowires	89
A.3	Semiconductor parameters for drift-diffusion simulations	93
A.4	Summary of optimization results for axial nanowire devices	96
B.1	Curve fit coefficients for energy capture efficiency	104
B.2	Radioisotope source properties	105
B.3	Intermediate results of best-case nanowire device efficiency calculation	107

List of Figures

2.1	Betavoltaic device geometry	15
2.2	Validation of energy deposition	17
2.3	Nanowire unit cell geometry	18
2.4	Correlation analysis of nanowire array parameters	21
2.5	Results of array optimization for GaP nanowires	22
3.1	Betavoltaic device schematic view	34
3.2	Optimum nanowire diameters	39
3.3	Example electron-hole pair generation rate profile	40
3.4	Comparison of energy capture efficiency to planar device	41
3.5	Optimum axial junction designs	44
3.6	Axial junction open-circuit voltage and short-circuit current	46
3.7	Optimum axial device performance	48
4.1	Optimized energy capture of nanowire arrays	62
4.2	Schematic representation of core-shell nanowire	64
4.3	Optimum core-shell junction designs	66
4.4	Optimum core-shell device performance	68
A.1	β source spectra	86
A.2	Optimum nanowire diameters	90

A.3	Comparison of nanowires to planar devices	92
A.4	IQE of axial nanowire devices	95
B.1	Complete curve fits of energy capture for optimized nanowire arrays .	104
B.2	The power density input for optimized nanowire arrays.	106

Notation & Abbreviations

BV Betavoltaic

EHP electron-hole pair

GaAs gallium arsenide

GaN gallium nitride

GaP gallium phosphide

IQE internal quantum efficiency

NW Nanowire

SC semiconductor

Si silicon

SiC silicon carbide

Preface & Declaration of Academic Achievement

This research was supported by the Natural Sciences and Engineering Research Council of Canada as well as The Department of Engineering Physics. This thesis includes the following three papers:

- **Paper I:** *Simulation & optimization of current generation in gallium phosphide nanowire betavoltaic devices*, D.L. Wagner, D.R. Novog, and R.R. LaPierre, Journal of Applied Physics 125, no. 16 (2019): 165704.
- **Paper II:** *Design & optimization of nanowire betavoltaic generators*, D.L. Wagner, D.R. Novog, and R.R. LaPierre, Journal of Applied Physics (submitted 2020).
- **Paper III:** *Genetic Algorithm Optimization of Core-Shell Nanowire Betavoltaic Generators*, D.L. Wagner, D.R. Novog, and R.R. LaPierre, Nanotechnology (submitted 2020).

The work presented in each paper required software development, simulations, design optimization, and data analysis; all of which represent original work completed solely by the author under the supervision of Dr. Dave Novog and Dr. Ray LaPierre.

Chapter 1

Introduction

1.1 Background

Despite the ubiquitous use of electrochemical cells, they continue to suffer from low energy densities, short discharge times, and environmental sensitivity. Betavoltaic (BV) generators, on the other hand, have been developed to circumvent these issues for low-power applications that require a long-lasting supply [1]. BVs function similarly to photovoltaics: electron-hole pairs (EHPs) are excited in a semiconductor (SC) p-n junction and collected to create electricity. However, unlike photovoltaics, BVs harness the energy from β particles as opposed to photons [2]. These β particles, products of some radioactive decay reactions, provide input energy to the device over the half-life of the radioisotope in question. In addition, because the kinetic energy of the β particles are on the order of keVs, thousands of EHPs can be generated from a single decay reaction. The particle flux, however, is much lower than that of solar photons so the overall device power output is on the order of nano/microwatts [3].

BVs remain useful for a variety of applications despite the lower power output.

Due to the long half-life of common BV sources (tens to hundreds of years), the low instantaneous power output is offset by the long discharge time, which results in an energy density much higher than that of electrochemical cells [4]. Therefore, BVs fill a unique niche in power supply technologies. Moreover, BVs are insensitive to environmental conditions which allows them to function at extreme temperatures or pressures without concern for malfunction or breakdown [5]. Such applications that benefit from BVs include biomedical implants, remote sensors, mobile microelectronics, and space exploration [1,6,7]. Challenges in these areas include infrequent access for maintenance, inability to rely on renewable sources (solar, wind), or exposure to conditions that would render electrochemical cells inoperable.

The design of BV generators can first be defined by the choice of radioisotope source. In this sense, the half-life and β decay energy (average *and* maximum) are important. The half-life of the material will define the overall lifetime of the generator and therefore a half-life long enough for a substantial energy density must be selected [8]. The decay energy, on the other hand, will determine the overall power density as well as survivability of the BV device. A higher β energy is desired to excite additional EHPs per reaction; however, above a certain energy threshold, β particles will begin to damage the SC lattice. Although this threshold is dependant on the SC, it is often quoted to be around 100 to 200 keV [1]. In addition to device functionality, certain applications may require that the source material is safe for users. Therefore, a pure β source (with no secondary reactions) is desired. β particles with energies less than 100 keV are easily shielded and are safe for human use [7]. Given these constraints, the most common radioisotopes used in BV applications are ^3H /tritium, ^{63}Ni , or ^{147}Pm [4]. Details on each source will be discussed in subsequent chapters.

In addition to the selection of the source, the SC converter must also be selected with several principles in mind. Similar to photovoltaics, many of the device performance metrics are governed by the SC material properties. The power conversion efficiency, which relies on the ability of the SC to collect the excited EHPs, is determined by characteristics such as carrier mobility, recombination effects, as well as the bandgap [9]. It has been shown that the ideal efficiency of the generator is proportional to the SC bandgap due to the higher open-circuit voltage possible with wide bandgap materials [10]. This will be discussed further in subsequent chapters. The SC must also be selected for radiation tolerance to mitigate the effects of lattice damage for higher energy β sources as mentioned previously. Some common SC materials include silicon (Si), silicon carbide (SiC), and gallium nitride (GaN) [4].

Lastly, the geometry of the generator plays a crucial role in the β collection efficiency. Conventional BV generators utilize a thin film source deposited on a thick, planar SC converter [11]. However, because β decay has an isotropic emission profile, only 50% of the input energy can be harnessed in this configuration. In an effort to surpass this drawback, a thicker radioisotope layer can be deposited on the SC or sandwiched between two converter layers. However, this is also limited due to source self-shielding (or the phenomena whereby radiation is shielded by the source itself), preventing additional energy from reaching the SC [12]. For this reason, the radioactivity (or input power) experienced by the SC saturates with a thicker source layer. Unique structuring techniques have been examined to mitigate the losses associated with self-shielding. Such structuring techniques exist to increase the surface area of the coupling interface between the SC and source, ensuring that more β particles interact with the active medium [3].

1.2 Literature Review

The initial development of BV devices began in the 1950's following the investigation of the BV effect in p-n junctions bombarded with β radiation [13]. This first device utilized a $^{90}\text{Sr}-^{90}\text{Y}$ compound source and was capable of achieving an output of 800 nW, an efficiency of 0.4%, and a predicted lifetime of 20 years [11]. However, the high decay energy of the radioisotope resulted in SC lattice damage, shifting development to focus on low energy radioisotopes [14].

In an attempt to mitigate the degradation issues from lattice damage, ^{147}Pm was investigated as a new source material. This led to the development of the first commercially available BV, Betacel, for use in pacemakers [2]. Betacel achieved a power output up to 400 μW , an efficiency of 4%, and was implanted in over 100 patients before the industry shifted attention to lithium-ion cells [1]. This shift away from the Betacel was mainly due to the high costs associated with shielding required for secondary gamma-rays produced by ^{146}Pm (a decay product of ^{147}Pm) [7].

It was also around this time that research began to investigate the benefits of wide and indirect bandgap SCs. It was determined that these SCs offered higher open-circuit voltages, efficiency, and radiation tolerance [2]. Although research in BVs became infrequent, the investigation into wide gap SCs and low-energy, pure β sources (^3H and ^{63}Ni) resulted in a resurgence of commercial viability. To date, there exists four main commercially available BV devices that are summarized in Table 1.1.

Currently, research into next-generation BV devices is focusing on micro- and nanostructuring as well as material engineering to improve β coupling, reduce effects of self-shielding, and further increase device efficiency. Research into porous SC media has been successful with Si and a gaseous tritium source whereby an order of

Table 1.1: Commercially available betavoltaic devices. Note that BetaBatt is currently under development. Efficiency ranges from 1 to 3%.

Device	SC Material	Activity	Source	Output Power
NanoTritium [1, 2]	Si compound	100 Ci	^3H	100 μW
BetaBatt [15–18]	Porous Si	8 Ci	Tritiated Butyl	6 μW
Fireffi-T [19]	Planar SiC	25 to 2500 mCi	^3H	10 to 1000 nW
Fireffi-N [19]	Planar SiC	5 to 500 mCi	^{63}Ni	5 to 500 nW

magnitude improvement in capture efficiency was observed [16–18]. Others have examined micro-pillar and inverted pyramid structures which have realized 50 to 100% increases to total device performance [20]. In addition, careful engineering of new materials has produced low-density and high activity sources that are promising for the development of high energy density devices [21, 22].

1.3 Motivation

Nanowires (NWs) are a unique method for achieving improvements to BVs with the next-generation techniques mentioned above. In addition to the high quality diodes that are possible with NW growth, source materials can be loaded between the NWs, potentially capturing more β particles. Previous work by McNamee investigated a prototype design whereby a gel containing ^{63}Ni was deposited between gallium phosphide (GaP) NWs via spin-coating [23]. Although it has been confirmed that these devices produced a β -generated current, the overall efficiency was less than 0.5%. This previous work highlighted that, although the fabrication method was valid for BV devices, the NW array and junction design required optimization to achieve competitive performance.

1.4 Goal & Outline of Thesis

The purpose of this thesis – the overall goal of this work – is to determine the optimum BV design of the NW architecture previously investigated by McNamee [23]. This optimum design would include the material choice (SC and source), array geometry, and junction design. Therefore, future experimental work on NW BVs can target the optimum designs predicted by this work and assess additional designs using the simulation methods developed herein.

This thesis is structured into three main chapters, besides the introduction and conclusion. Each of the body chapters corresponds to a published article that is self-contained with respect to the work described therein. Chapter 2 presents a verification of the energy capture simulations and outlines the method for determining the optimum NW array geometry. Chapter 3 expands the array optimization to several potential device designs and couples the energy capture simulations to SC charge-transport calculations in axial p-i-n NWs. The methods outlined in Chapter 3 are the first established for the complete (fully-coupled) modeling of NW BVs. Lastly, Chapter 4 highlights improvements to the results of Chapter 3 by utilizing core-shell NWs and presents the best-case device performance for this architecture.

As mentioned, the body chapters are stand-alone works and therefore, there is overlap in the introduction to BVs discussed for each. Particularly, the governing equations for device efficiency as well as the fundamentals of BV design are discussed throughout.

References

- [1] L. C. Olsen, P. Cabaay, and B. J. Elkind, “Betavoltaic power sources,” *Physics Today*, vol. 65, no. 12, pp. 35–38, 2012.
- [2] L. C. Olsen, “Betavoltaic energy conversion,” *Energy Conversion*, vol. 13, no. 4, pp. 117–127, 1973.
- [3] T. R. Alam and M. A. Pierson, “Principles of Betavoltaic Battery Design,” *J. Energy Power Sources*, vol. 3, no. 1, pp. 11–41, 2016.
- [4] M. A. Prelas, C. L. Weaver, M. L. Watermann, E. D. Lukosi, R. J. Schott, and D. A. Wisniewski, “A review of nuclear batteries,” *Progress in Nuclear Energy*, vol. 75, no. December 2017, pp. 117–148, 2014.
- [5] G. R. Ghasemi Nejad, F. Rahmani, and G. R. Abaeiani, “Design and optimization of beta-cell temperature sensor based on $^{63}\text{Ni-Si}$,” *Applied Radiation and Isotopes*, vol. 86, pp. 46–51, 2014.
- [6] P. E. Sims, L. C. Dinetta, and A. M. Barnett, “High efficiency GaP power conversion for betavoltaic Applications,” *NASA. Lewis Research Center, Proceedings of the 13th Space Photovoltaic Research and Technology Conference*, vol. 13, pp. 373–382, 1994.
- [7] T. Smith, J. Greenborg, and W. Matheson, “Benefit/risk analysis of cardiac pacemakers powered by betacel® promethium-147 batteries,” *Nuclear Technology*,

- vol. 26, no. 1, pp. 54–64, 1975.
- [8] F. K. Manasse, J. J. Pinajian, and A. N. Tse, “Schottky barrier betavoltaic battery,” *IEEE Transactions on Nuclear Science*, vol. 23, no. 1, pp. 860–870, 1976.
- [9] A. V. Sachenko, A. I. Shkrebtii, R. M. Korkishko, V. P. Kostylyov, M. R. Kulish, and I. O. Sokolovskyi, “Efficiency analysis of betavoltaic elements,” *Solid-State Electronics*, vol. 111, pp. 147–152, 2015.
- [10] C. A. Klein, “Bandgap dependence and related features of radiation ionization energies in semiconductors,” *Journal of Applied Physics*, vol. 39, no. 4, pp. 2029–2038, 1968.
- [11] P. Rappaport, “The electron-voltaic effect in p- n junctions induced by beta-particle bombardment,” *Physical Review*, vol. 93, no. 1, p. 246, 1954.
- [12] J. Russo, M. Litz, W. Ray, G. M. Rosen, D. I. Bigio, and R. Fazio, “Development of tritiated nitroxide for nuclear battery,” *Applied Radiation and Isotopes*, vol. 125, no. March, pp. 66–73, 2017.
- [13] P. Rappaport and E. G. Linder, “Radioactive charging effects with a dielectric medium,” *Journal of Applied Physics*, vol. 24, no. 9, pp. 1110–1114, 1953.
- [14] W. Pfann and W. Van Roosbroeck, “Radioactive and photoelectric p-n junction power sources,” *Journal of Applied Physics*, vol. 25, no. 11, pp. 1422–1434, 1954.
- [15] L. L. Gaden, W. Sun, N. P. Kherani, P. M. Fauchet, and K. D. Hirschman, “Methods of making energy conversion devices with a substantially contiguous depletion regions,” July 31 2007. US Patent 7,250,323.
- [16] W. Sun, N. P. Kherani, K. D. Hirschman, L. L. Gaden, and P. M. Fauchet, “A three-dimensional porous silicon p-n diode for betavoltaics and photovoltaics,”

- Advanced Materials*, vol. 17, no. 10, pp. 1230–1233, 2005.
- [17] J. P. Clarkson, W. Sun, K. D. Hirschman, L. L. Gadeken, and P. M. Fauchet, “Betavoltaic and photovoltaic energy conversion in three-dimensional macroporous silicon diodes,” *Physica Status Solidi (A) Applications and Materials Science*, vol. 204, no. 5, pp. 1536–1540, 2007.
- [18] B. Liu, K. P. Chen, N. P. Kherani, and S. Zukotynski, “Power-scaling performance of a three-dimensional tritium betavoltaic diode,” *Applied Physics Letters*, vol. 95, no. 23, pp. 1–4, 2009.
- [19] A. L. M.V.S. Chandrashekar, Christopher I. Thomas, Hui Li, M.G. Spencer, “Demonstration of a 4H SiC betavoltaic cell,” *Applied Physics Letters*, vol. 88, 2006.
- [20] J. Russo, M. S. Litz, I. I. William Ray, H. Berk, H. Cho, D. I. Bigio, A. Wertz, and T. R. Alam, “Planar and textured surface optimization for a tritium-based betavoltaic nuclear battery,” *International Journal of Energy Research*, vol. 43, no. 9, pp. 4370–4389, 2019.
- [21] T. R. Alam, M. G. Spencer, M. A. Prelas, and M. A. Pierson, “Design and optimization of radioisotope sources for betavoltaic batteries,” *International Journal of Energy Research*, vol. 42, no. 7, pp. 2564–2573, 2018.
- [22] C. Thomas, S. Portnoff, and M. G. Spencer, “High efficiency 4H-SiC betavoltaic power sources using tritium radioisotopes,” *Applied Physics Letters*, vol. 108, no. 1, pp. 1–5, 2016.
- [23] S. McNamee, D. Wagner, E. Fiordaliso, D. Novog, and R. LaPierre, “GaP nanowire betavoltaic device,” *Nanotechnology*, vol. 30, no. 7, 2019.

Chapter 2

Optimization of Energy Capture

In order to combat the effects of self-shielding in BV devices, a device architecture utilizing NWs is presented. Monte Carlo simulations are used to calculate the energy capture of GaP devices to confirm the improvements that the NW geometry offers. Also, it is determined that the NW array geometry (diameter and pitch) are significant design parameters and can be optimized for maximum β capture. A method for optimizing the array is presented and predicted improvement factors with various radioisotopes are used to select promising sources for future investigation. In addition, the array optimization is established as an important first step in determining the best device configuration.

Simulation and optimization of current generation in gallium phosphide nanowire betavoltaic devices

DOI: 10.1063/1.5093805

Reproduced from:

D. Wagner, D. R. Novog, and R. R. LaPierre, "Simulation and optimization of current generation in gallium phosphide nanowire betavoltaic devices," *Journal of Applied Physics*, vol. 125, no. 16, 2019.

...with the permission of AIP Publishing

ABSTRACT: The geometry of a gallium phosphide nanowire array has been optimized for maximum current generation in a betavoltaic device. The energy capture efficiency for various device geometries with different radioisotope source compounds was calculated in GEANT4. A validation of GEANT4 for betavoltaic device simulation was performed by comparing a model output with the available bulk SC betavoltaic performance data, followed by predictions of the performance of nanowire-based devices. The pitch and the diameter of the nanowires were found to have the most significant impact on the β -generated current density, with the optimum diameter-to-pitch ratios ranging from 0.55 to 0.8, depending on the source. The energy capture efficiency improved when low energy β emitters were used. For devices utilizing ^{63}Ni source compounds, the β -generated current densities approached $0.95 \mu\text{A cm}^{-2}$, representing an improvement by a factor as high as 5.8 compared to planar devices. In the case of ^3H source compounds, the generated current density was $3.05 \mu\text{A cm}^{-2}$, a factor of 15.5 larger than comparable planar devices. However, nanowire devices utilizing sources with a higher decay energy, such as ^{147}Pm , did not demonstrate any improvements over planar geometries. Using the results for optimum nanowire geometries, nanowire-based or other nanostructured devices could be made to surpass the present commercial betavoltaic batteries.

2.1 Introduction

Despite the ubiquitous use of electrochemical batteries, they suffer from limited lifetimes, high sensitivity to environmental conditions, and low specific energy. BV batteries have therefore been developed for micro-/nano-applications, which provide a long-lasting (up to hundreds of years), steady supply of power that cannot be provided by conventional energy storage devices [1]. BVs provide electrical energy through the production of EHPs in a semiconducting material, similar to the operation of photovoltaic devices. However, in a BV generator, the EHPs are excited through impact ionization from β -particles originating in the nuclear decay of some radioactive isotopes [2]. These β -particles can have energies in the range of several keV and, therefore, a single β -particle can excite thousands of EHPs as it thermalizes through the SC lattice. Unfortunately, the long half-life (low decay rate) results in a particle flux that is orders of magnitude lower than that of solar photons. Therefore, BVs demonstrate low (ranges on the order of nW cm^{-2} to $\mu\text{A cm}^{-2}$) power densities [3]. Despite the low power output of these devices, they are able to operate autonomously across a wide range of conditions, making them ideal for applications in mobile electronics, space exploration, remote sensing, and implantable biomedical devices [4]. As discussed below, the efficiency of BV cells could be further improved by implementing SC NWs in place of thin film or bulk SCs, thereby improving the energy output or device life as compared to conventional BV cells. The goal of this work is the validation of GEANT4 code for the simulation of BV devices, and the determination of the limiting performance of NW-based versus bulk SC BV devices.

Conventional BV devices are designed with a layer of radioisotope deposited on a thick planar SC substrate. However, because the radioactive emission is isotropic,

approximately half of all β -particles do not contribute to energy conversion. This design also limits the flux of incident particles on the SC surface due to a combination of shielding from the device contacts and the self-shielding from the source material itself [5]. These limitations can be mitigated by the utilization of higher energy (≈ 100 s of keV) β sources to increase transmission through the shielding materials, although this has also been shown to limit device lifetime as this energy is on the order of the lattice damage threshold for most SCs [3]. It is therefore important to select radioisotopes whose maximum and average energies (E_{max} and \bar{E} , respectively) are of the correct range. For this reason, practical radioisotope sources consist mainly of ^{63}Ni ($E_{max} = 65.90$ keV, $\bar{E} = 17.43$ keV), or tritium/ ^3H ($E_{max} = 18.60$ keV, $\bar{E} = 5.70$ keV) compounds. Some devices also utilize ^{147}Pm ; however, the higher β energies ($E_{max} = 230.0$ keV, $\bar{E} = 62.0$ keV) result in higher lattice damage within the SC and hence shorter device lifetimes [6].

BV performance is governed by two quantities: the energy capture efficiency, η_{ec} , which quantifies the amount of radioisotope energy deposited into the SC material, and the SC efficiency, η_s , which is a combination of diode performance and material parameters [7]. The overall energy conversion efficiency is given by:

$$\eta = \eta_{ec}\eta_s. \quad (2.1)$$

Here, η_s can be calculated as:

$$\eta_s = \frac{q \cdot FF \cdot V_{oc} \cdot Q}{\varepsilon}, \quad (2.2)$$

where q is the elementary charge, FF is the fill-factor of the diode, V_{oc} is the open-circuit voltage, Q is the EHP collection efficiency, and ε is the ionization energy (or the average energy required to produce a single EHP). With ideal device operation, Equation 2.2 approaches E_g/ε , which is often quoted as the limiting BV device efficiency for a given SC material [4]. It is therefore evident that high bandgap SCs are ideal for highly efficient devices.

In addition to utilizing high bandgap materials, devices can be structured to surround the radioisotope to improve the energy capture efficiency in Equation 2.1. The technique of nanostructuring has been demonstrated with porous silicon utilizing a tritium source, and has exhibited performance improvements by up to a factor of ten over planar devices [8–10]. However, this could be further improved through the utilization of higher bandgap materials such as GaP, corresponding to higher BV cell voltage as per Equation 2.2. The growth of Group III-V compound SC NWs to surround radioisotopes introduces an opportunity for significant improvement to BV performance by simultaneously increasing energy capture and SC efficiencies with high bandgap materials. A comparison of conventional, planar BV geometry and the proposed NW geometry is shown in Figure 2.1, highlighting the various loss mechanisms and absorption paths for β -particles discussed below.

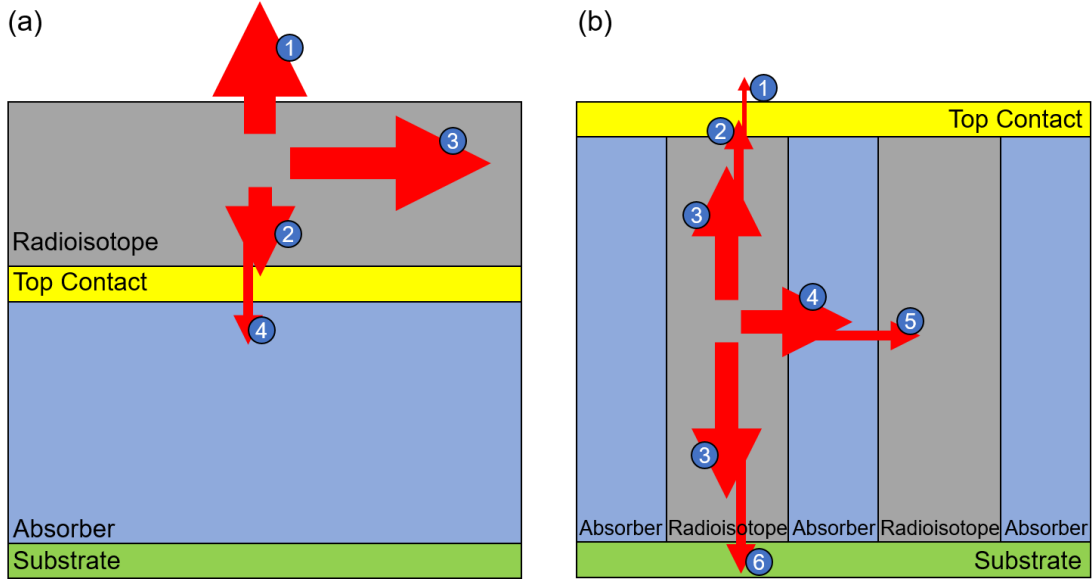


Figure 2.1: Cross-sectional view of BV geometry for (a) planar devices and (b) NW devices. Not to scale. The β -particles are shown 1) escaping, 2) shielded by the contact, 3) shielded by the radioisotope (self-shielding), 4) absorbed in the active device volume, 5) transmitted through the active device volume, and 6) absorbed by the substrate. The relative magnitude of each is depicted by the thickness of the corresponding arrows.

GaP ($\varepsilon = 7.8 \text{ eV}$ [11]) is a good candidate material for BV devices due to its large bandgap (corresponding to a large output voltage), and GaP NWs are easily grown using the vapor-liquid-solid method [12,13]. However, prototype efficiencies for these NW devices have only reached approximately 0.5% [13]. In the present work, we demonstrate the use of GEANT4 as a method for simulating the energy capture in BV devices to improve future BV performance.

2.2 Modeling Energy Capture

The energy capture efficiency as outlined in Equation 2.1 can be determined through Monte-Carlo simulations. These simulations model the tracks of β -particles and their interaction (energy deposition) with various materials within the device. The GEANT4 nuclear particle interaction toolkit [14] was utilized for these simulations. The initial energy of each primary particle (β) was sampled from the specified radioisotope emission spectrum and initiated at a random location within the source material and with random direction. It is then tracked through various scattering interactions, the probabilities of which are governed by the Livermore low energy dataset [15]. The energy deposited in each interaction is distributed between each domain, effectively calculating the linear energy deposition within any given volume. The energy deposition profiles for common BV SCs (SiC, Si, and GaN) are calculated for the energy spectra of the three radioisotopes mentioned above (^{63}Ni , ^3H , and ^{147}Pm). The results, as compared to examples from literature, are shown in Figure 2.2. The agreement between our simulations (circles) and literature [16–18] (solid lines) were within 5%, indicating that the method within GEANT4 and the selection of the material dataset are both justified.

In addition to the energy deposition, GEANT4 can also be used to calculate the total β -generated current density, J_β , from η_{ec} . The two are related through

$$J_\beta = \frac{q \cdot N \cdot E}{\varepsilon} \eta_{ec}, \quad (2.3)$$

where N is the total activity density of the source deposited on the device (in Bq cm^{-2}) and E is the energy of the incident β -particles [19]. With a sufficiently large number

of particle histories, the value of E will approach the mean source energy, \bar{E} . For an ideal diode (*i.e.* $Q = 1$), Equation 2.3 approximates the short-circuit current density, J_{sc} , of the device. Table 2.1 compares the value of the β -generated current density calculated in GEANT4 (J_{β}^{sim}) to measurements reported in literature (J_{β}) for the case of planar devices using GaN, Si, and 4H-SiC (where the value of ε is taken from the associated reference). Our simulations show excellent agreement with the literature values.

Given that the method outlined above has been validated for several planar devices, it can also be extended to non-conventional geometries such as the GaP NW array shown in Figure 2.3.

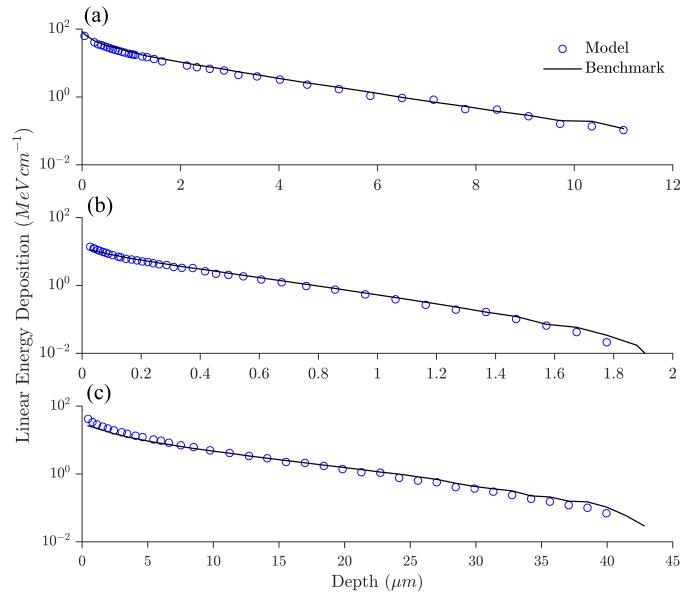


Figure 2.2: Simulated (circles) linear deposition profiles compared to results in literature (solid lines) for (a) ^{63}Ni on SiC [16], (b) ^3H on Si [17] and (c) ^{147}Pm on GaN [18].

Table 2.1: β -generated current density calculation compared to literature values

Device	Activity Density (mCi cm ⁻²)	η_{ec} (%)	J_{β}^{sim} (nA cm ⁻²)	J_{β} (nA cm ⁻²)
⁶³ Ni on GaN [20]	25.0	4.74	11.9	12.0
¹⁴⁷ Pm ₂ O ₃ on Si [21]	1200	28.3	34603	35000
Si ³ H _{1.66} on 4H-SiC [22]	93.8	17.2	74.9	75.5

The array geometry is modeled as a single, non-primitive hexagonal unit cell with the radioisotope source filling the voided area between the NWs. A 25 μm thick Si substrate (sufficiently thick for 100% β absorption) and 25/50/225 nm thick nickel/germanium/gold top contact (a typical n-type contact for Group III-V compounds) were also included in the model. The NWs extend 200 nm deep into the top contact material, which is typical for NW devices (hence, the constraint in Equation 2.4 below). Periodic boundary conditions are set on the sidewalls of the unit cell to simulate the semi-infinite behaviour of the NW array. This geometry has also been used to verify the energy capture efficiency of our previous devices [13].

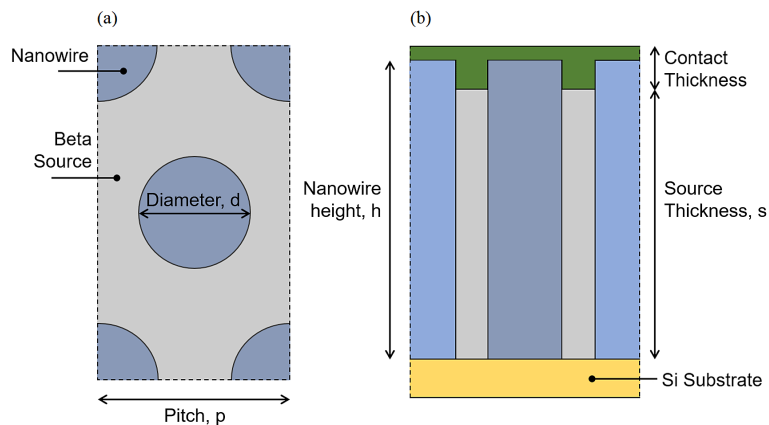


Figure 2.3: The NW unit cell geometry modeled in GEANT4 shown from (a) the top and (b) the side. Dashed lines indicate periodic boundary conditions. Not to scale.

2.3 Nanowire Geometry Optimization

To optimize the geometry of the GaP NW arrays, the β -generated current density was investigated as the objective (maximization) function. This was chosen as the objective over solely the energy capture efficiency, as maximizing both the energy deposition and source volume is desirable to produce a device with the highest output power. The four geometric parameters to be optimized, as shown in Figure 2.3, are the pitch, diameter, and height of the NWs as well as the thickness of the source material (p , d , h and s , respectively). The range of parameter values considered were:

$$100 \text{ nm} \leq h \leq 10 \text{ }\mu\text{m} \quad (2.4)$$

$$100 \text{ nm} \leq p \leq 1 \text{ }\mu\text{m} \quad (2.5)$$

$$50 \text{ nm} \leq d \leq 1 \text{ }\mu\text{m} \quad (2.6)$$

$$100 \text{ nm} \leq s \leq 10 \text{ }\mu\text{m} \quad (2.7)$$

$$d \leq p - 100 \text{ nm} \quad (2.8)$$

$$s \leq h - 200 \text{ nm} \quad (2.9)$$

These bounds were set by the practical limitations of NW growth and device fabrication techniques. For cases where the NW height was larger than the source thickness, a bisbenzocyclobutene polymer encapsulation was used to fill the remaining void [13]. It should also be noted that the geometries modeled here assume negligible GaP thin film thickness at the base of the NWs, which would absorb additional β energy while not contributing to overall device performance [23]. Negligible thin film growth is achievable in certain growth modes, such as axial vapour-liquid-solid growth of NWs [24]. Such NWs have also demonstrated superior diode performance

in photovoltaic applications [24]. The DAKOTA optimization toolkit [25] was used to perform parameter sweeps across the entire feasible range of inputs for the three radioisotope spectra of interest. A partial correlation analysis [26] was then performed to assess the individual contribution of each parameter to the overall objective function while holding the other three fixed. These results are shown in Figure 2.4. From this analysis, the NW height alone (while keeping the source thickness, s , constant) had little impact on the overall current density generated in the device, with its contribution being directly proportional to the β particle energy of the source isotope in question. In addition, the generated current density is nearly directly correlated with source thickness as expected due to the higher activity present in the device. Therefore, it is apparent that an optimum device would utilize NWs grown as tall as possible only to accommodate the most source material. This is consistent with previous simulation results [13]. However, the NW pitch and diameter exhibited a competing contribution with almost equal and opposite correlations. Again, this is expected due to the inverse relationship between absorber and source volumes. The array should therefore be optimized for the NW pitch and diameter while setting the height and source thickness to $10\ \mu\text{m}$ and $9.8\ \mu\text{m}$, respectively (within the constraints of Equation 2.5 and Equation 2.7). By maximizing the source volume as per Equation 2.9, device current density should continue to scale linearly for arbitrarily long NWs (ignoring carrier recombination) because of the additional device activity and minimum self-shielding effects between NWs.

Given the feasible range for the pitch and diameter of the NWs outlined above, the geometry was optimized using two source compounds for each of the radioisotopes previously outlined. Pure sources (tritium gas as well as elemental ^{63}Ni and

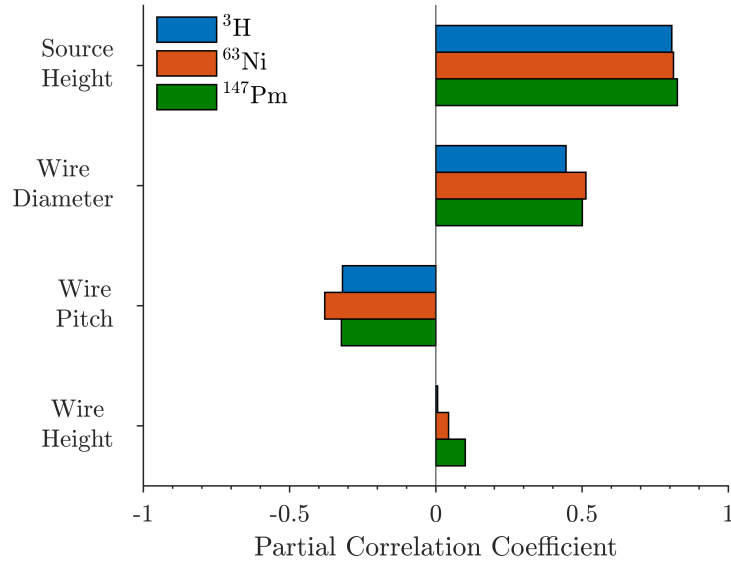


Figure 2.4: Results of the partial correlation analysis between β -generated current density and nanowire array geometric parameters.

^{147}Pm) were used to provide a reference for common compounds containing the radioactive isotopes. These compounds include tritiated butyl [27], trinickel-dicitrate (Ni-Cit) [13], and promethium-oxide [22]. For each source material, an optimum $d : p$ ratio was found (Figure 2.5a to c) with a clear Gaussian relationship evident. The Gaussian relationships in Figure 2.5 were found using a Nelder-Mead simplex search minimization routine [28]. An optimum $d : p$ ratio for each source material implies that the radiation length (the β -particle range of a given energy in a given material) is crucial when designing the NW arrays. This is also consistent with the principle of length scale matching for BV battery design; *i.e.* energy capture efficiency will be maximized when the range of β -particles is comparable to the length scale of the device [29]. Figure 2.5d shows the optimum device power densities and energy densities

assuming ideal diode conditions ($Q = 1$, $FF = 1$, $qV_{oc} = E_g$). Although the ^{147}Pm devices seem to perform well, this is merely due to the high decay energies. However, ^{147}Pm yields a device with a much shorter half-life of 2.6 y as compared to ^{63}Ni or ^3H devices (whose half-lives are 101.3 y and 12.3 y, respectively). As mentioned earlier, the high beta energies of ^{147}Pm are also near the lattice damage threshold of most SCs and therefore may result in SC deterioration.

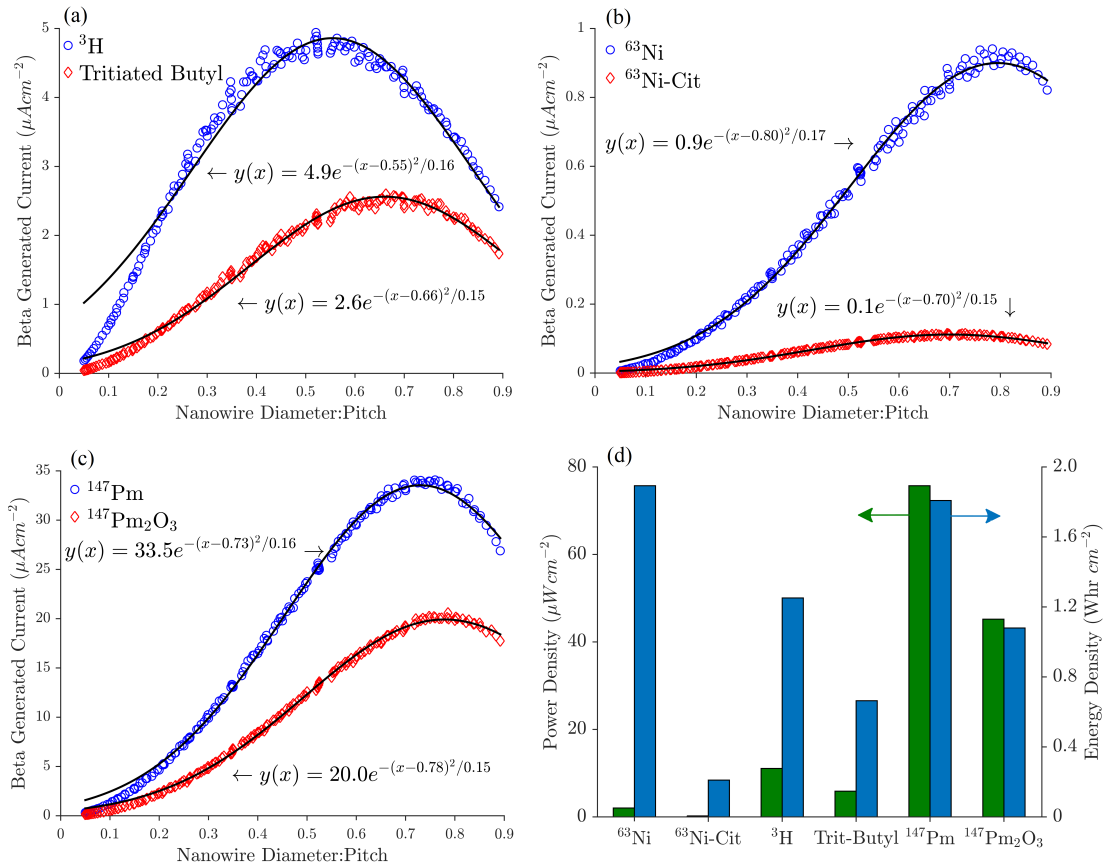


Figure 2.5: Optimization results for GaP NW arrays filled with (a) tritium, (b) ^{63}Ni and (c) ^{147}Pm sources. Gaussian fits are shown. (d) The resulting power and energy densities.

Table 2.2: β -generated current density for the optimum NW geometries compared to a planar device with the same input power

Source Material	Optimized Geometry (nm)		Input Power ($\mu\text{W cm}^{-2}$)	η_{ec} (%)		J_{β}^{sim} ($\mu\text{A cm}^{-2}$)		Improvement Factor
	Pitch	Diameter		Wires	Planar	Wires	Planar	
^{63}Ni	500	400	21.2	35.0	5.16	0.95	0.14	5.8
$^{63}\text{Ni-Cit}$	333	233	1.95	44.8	13.5	0.11	0.03	2.3
$^3\text{H}_2$	222	122	57.0	69.2	10.9	5.06	0.81	5.3
Tritiated Butyl	294	194	47.6	50.0	3.03	3.05	0.18	15.5
^{147}Pm	370	270	1255	21.0	23.3	33.7	37.5	-0.10
$^{147}\text{Pm}_2\text{O}_3$	455	355	881	17.4	20.4	19.6	23.0	-0.15

Optimum d and p values were determined by using the optimum $d : p$ ratios outlined in Figure 2.5 and the constraint in Equation 2.8. A comparison between the NW array devices and planar devices is made in Table 2.2. The thickness of the source used in the planar devices was varied such that the power input was equivalent to that in the corresponding optimum NW device. This allowed for a direct assessment of the improvement in device performance that the NW geometries are able to provide. For lower energy sources (^{63}Ni and ^3H), the improvement is large (5.8- or 15.5-fold, respectively), illustrating the benefit of nanostructuring for energy capture and the mitigation of shielding effects. This is made clear by examining the low energy capture efficiencies for the planar cases; to achieve a high input power, the radioisotope layer must have a thickness on the order of microns which results in large shielding losses in addition to the 50% loss due to isotropic emission. However, in higher energy regimes such as with the ^{147}Pm sources, transmission loss of the β -particles dominates and hence, there are no performance improvements obtained by utilizing nanostructured SCs.

2.4 Conclusions

The potential for high performance NW BV devices has been demonstrated through the optimization of β -generated current density calculated via GEANT4 Monte-Carlo simulations. For devices utilizing ^{63}Ni and ^3H sources, length-matching of the NW diameter and pitch to the path length of the β -particles provides an opportunity for increased energy capture efficiency. The β -generated current densities for devices utilizing ^{63}Ni , $^{63}\text{Ni-Cit}$, $^3\text{H}_2$ gas, and tritiated butyl, demonstrate an improvement factor of 5.8, 2.3, 5.3, and 15.5, respectively, over the planar device counterparts. However, devices based on ^{147}Pm sources did not demonstrate any improvements which is due largely to the high energy β -particles not being absorbed on the length scale of the NWs.

Future work will couple the energy deposition simulation results to SC charge transport models to provide an accurate estimate for overall device performance and power generation. Various aspects such as SC dopant profiles and NW growth morphologies (axial versus radial p-n junctions) can be examined as an additional parameter for optimization. In addition, other candidate SC materials (Si, SiC, GaN, *etc.*) will be investigated.

References

- [1] F. K. Manasse, J. J. Pinajian, and A. N. Tse, “Schottky barrier betavoltaic battery,” *IEEE Transactions on Nuclear Science*, vol. 23, no. 1, pp. 860–870, 1976.
- [2] P. Rappaport and E. G. Linder, “Radioactive charging effects with a dielectric medium,” *Journal of Applied Physics*, vol. 24, no. 9, pp. 1110–1114, 1953.
- [3] L. C. Olsen, P. Cabaay, and B. J. Elkind, “Betavoltaic power sources,” *Physics Today*, vol. 65, no. 12, pp. 35–38, 2012.
- [4] S. T. Revankar and T. E. Adams, “Advances in Betavoltaic Power Sources,” *Journal of Energy and Power Sources*, vol. 1, no. 6, pp. 321–329, 2014.
- [5] L. C. Olsen, “Betavoltaic energy conversion,” *Energy Conversion*, vol. 13, no. 4, pp. 117–127, 1973.
- [6] M. A. Prelas, C. L. Weaver, M. L. Watermann, E. D. Lukosi, R. J. Schott, and D. A. Wisniewski, “A review of nuclear batteries,” *Progress in Nuclear Energy*, vol. 75, no. December 2017, pp. 117–148, 2014.
- [7] A. V. Sachenko, A. I. Shkrebtii, R. M. Korkishko, V. P. Kostylyov, M. R. Kulish, and I. O. Sokolovskyi, “Efficiency analysis of betavoltaic elements,” *Solid-State Electronics*, vol. 111, pp. 147–152, 2015.

- [8] J. P. Clarkson, W. Sun, K. D. Hirschman, L. L. Gadeken, and P. M. Fauchet, “Betavoltaic and photovoltaic energy conversion in three-dimensional macroporous silicon diodes,” *Physica Status Solidi (A) Applications and Materials Science*, vol. 204, no. 5, pp. 1536–1540, 2007.
- [9] B. Liu, K. P. Chen, N. P. Kherani, and S. Zukotynski, “Power-scaling performance of a three-dimensional tritium betavoltaic diode,” *Applied Physics Letters*, vol. 95, no. 23, pp. 1–4, 2009.
- [10] W. Sun, N. P. Kherani, K. D. Hirschman, L. L. Gadeken, and P. M. Fauchet, “A three-dimensional porous silicon p-n diode for betavoltaics and photovoltaics,” *Advanced Materials*, vol. 17, no. 10, pp. 1230–1233, 2005.
- [11] B. Goldstein, “Electron-hole pair creation in gallium phosphide by α particles,” *Journal of Applied Physics*, vol. 36, no. 12, pp. 3853–3856, 1965.
- [12] P. Sims and L. C. DiNetta, “Gallium phosphide energy converters,” *Space Photovoltaic Research and Technology*, 1995.
- [13] S. McNamee, D. Wagner, E. Fiordaliso, D. Novog, and R. LaPierre, “GaP nanowire betavoltaic device,” *Nanotechnology*, vol. 30, no. 7, 2019.
- [14] S. Agostinelli *et al.*, “GEANT4 – a simulation toolkit,” *Nuclear Instruments and Methods in Physics Research Section A: Accelerators, Spectrometers, Detectors and Associated Equipment*, vol. 506, no. 3, pp. 250–303, 2003.
- [15] T. Toshito *et al.*, “Validation of New Geant4 Electromagnetic Physics Models for Ion Therapy Applications,” *Progress in Nuclear Science and Technology*, vol. 2, no. 0, pp. 918–922, 2011.
- [16] S. Theirrattanakul and M. Prelas, “A methodology for efficiency optimization

- of betavoltaic cell design using an isotropic planar source having an energy dependent beta particle distribution,” *Applied Radiation and Isotopes*, vol. 127, no. December 2016, pp. 41–46, 2017.
- [17] M. Wu, S. Wang, Y. Ou, and W. Wang, “Optimization design of betavoltaic battery based on titanium tritide and silicon using Monte Carlo code,” *Applied Radiation and Isotopes*, vol. 142, no. September, pp. 22–27, 2018.
- [18] X. Tang, Y. Liu, D. Ding, and D. Chen, “Optimization design of GaN betavoltaic microbattery,” *Science China Technological Sciences*, vol. 55, no. 3, pp. 659–664, 2012.
- [19] R. Bao, P. J. Brand, and D. B. Chrisey, “Betavoltaic performance of radiation-hardened high-efficiency Si space solar cells,” *IEEE Transactions on Electron Devices*, vol. 59, no. 5, pp. 1286–1294, 2012.
- [20] Z. Cheng, H. San, Z. Feng, B. Liu, and X. Chen, “High open-circuit voltage betavoltaic cell based on GaN pin homojunction,” *Electronics Letters*, vol. 47, no. 12, p. 720, 2011.
- [21] L. S. Wei, “Parametric studies and optimization of the betavoltaic cell-II open-circuit voltage and power efficiencies BETAVOLTAIC CELL-II OPEN-CIRCUIT VOLTAGE AND POWER EFFICIENCIES,” *Solid State Electronics*, vol. 18, pp. 71–77, 1975.
- [22] C. Thomas, S. Portnoff, and M. G. Spencer, “High efficiency 4H-SiC betavoltaic power sources using tritium radioisotopes,” *Applied Physics Letters*, vol. 108, no. 1, pp. 1–5, 2016.
- [23] C. M. Haapamaki, J. Baugh, and R. R. LaPierre, “Facilitating growth of InAsInP coreshell nanowires through the introduction of Al,” *Journal of Crystal Growth*,

- vol. 345, no. 1, pp. 11–15, 2012.
- [24] G. Otnes and M. T. Borgström, “Towards high efficiency nanowire solar cells,” *Nano Today*, vol. 12, pp. 31–45, 2017.
- [25] T. Trucano *et al.*, “Dakota, A Multilevel Parallel Object-Oriented Framework for Design Optimization, Parameter Estimation, Uncertainty Quantification, and Sensitivity Analysis,” tech. rep., Sandia National Laboratories, 2014.
- [26] B. Iooss and P. Lemaître, “A review on global sensitivity analysis methods,” *Operations Research/ Computer Science Interfaces Series*, vol. 59, no. around 30, pp. 101–122, 2015.
- [27] P. E. Sims, L. C. Dinetta, and A. M. Barnett, “High efficiency GaP power conversion for betavoltaic Applications,” *NASA. Lewis Research Center, Proceedings of the 13th Space Photovoltaic Research and Technology Conference*, vol. 13, pp. 373–382, 1994.
- [28] J. C. Lagarias, J. A. Reeds, M. H. Wright, and P. E. Wright, “Convergence properties of the nelder–mead simplex method in low dimensions,” *SIAM Journal on optimization*, vol. 9, no. 1, pp. 112–147, 1998.
- [29] J. Dixon, A. Rajan, S. Bohlemann, D. Coso, A. D. Upadhyaya, A. Rohatgi, S. Chu, A. Majumdar, and S. Yee, “Evaluation of a Silicon 90 Sr Betavoltaic Power Source,” *Scientific Reports*, vol. 6, pp. 4–9, 2016.

Chapter 3

Coupled Simulation for Total Power Optimization

The radiation capture simulations presented in Chapter 2 are coupled to drift-diffusion calculations in order to optimize junction design and determine total device power for axial p-i-n devices. Furthermore, the method previously presented is expanded to additional design combinations in order to examine the energy capture performance for a range of SCs and the corresponding optimum array geometry. By highlighting the energy capture for the NW devices, it is determined that self-shielding does not impact performance as seen with planar devices. Due to this increased energy capture efficiency, total device performance of NW BVs is predicted to compete with top-performing devices in literature. However, performance of long NWs (specifically GaP) is limited due to surface recombination. Therefore, there exists the opportunity to still further improve the NW device architecture.

Design and Optimization of Nanowire Betavoltaic Generators

DOI: 10.1063/1.5138119

Reproduced from:

D. Wagner, D. R. Novog, and R. R. LaPierre, "Design and Optimization of Nanowire Betavoltaic Generators," *Journal of Applied Physics*, vol. 128, no. 1, 2020.

...with the permission of AIP Publishing

ABSTRACT: A model used to simulate and optimize the performance of nanowire-based betavoltaic generators is developed. The optimum nanowire array geometry is established for devices made of silicon, gallium arsenide, and gallium phosphide for both nickel-63 and tritium sources by computing the energy capture efficiency for each case. The captured power for nanowire devices is shown to be drastically greater compared to planar betavoltaic generators with maximum improvement factors of approximately 7, 3, 5 and 9 for devices utilizing radioisotope sources of nickel-63, nickel citrate, tritium and tritiated butyl, respectively. In addition, nanowire devices do not suffer from self-shielding effects, a large limitation in conventional, planar betavoltaics. By coupling the spatial distribution of electron-hole pair generation rate calculated from Monte Carlo simulations and a SC charge-transport model, the diode design is optimized for maximum power output. The top performing devices, utilizing a tritium source, exhibited an output power of approximately 4, 6 and 2 $\mu\text{W cm}^{-2}$ for silicon, gallium arsenide and gallium phosphide, respectively. Overall device efficiencies were found to range from 4 to 10%, surpassing several betavoltaic devices reported in literature. It was also found that, contrary to traditional betavoltaic design, SCs with higher bandgaps do not necessarily result in the best device performance due to additional material parameters, such as surface recombination velocity. Potential improvements for nanowire-based betavoltaic generators are suggested for additional investigation.

3.1 Introduction

Mobile applications, which require a low power and long-lasting source, suffer from limitations with conventional electrochemical cells due to challenges with scalability, stability, and lifetimes [1]. Such requirements exist in the fields of space exploration, remote sensing, personal electronics and biomedical implants, or other instances where frequent power source replacement and the utilization of other sources is not feasible [2]. BV generators, or nuclear batteries, are potential power supplies for such applications. These BV devices are composed of a SC converter and a radioisotope source, which decays and emits β particles [3, 4]. The energy conversion mechanism is similar to that in photovoltaic devices, where the electrical work provided by the device is delivered by excited EHPs in the SC medium; however, the kinetic energy of emitted β particles is harnessed in BV devices, as compared to the harvesting of solar photon energy in photovoltaic devices. The β particles, with energy on the order of keV, inelastically collide with the SC lattice which can create thousands of EHPs through impact ionization. The resulting output current from these interactions is on the order of nA cm^{-2} to $\mu\text{A cm}^{-2}$ [5, 6].

The performance of BV devices is a function of radioisotope source characteristics, device geometry, and properties of the SC converter. Where the radioisotope half-life alone determines the ultimate device lifetime, both the activity (the rate of decay multiplied by the number of radioactive atoms present) and the average β -decay energy dictates the total power input driving the generator. Additionally, to maximize the coupling (deposition) of β -energy into the SC, the β particle penetration depth should be on the same scale as the SC dimensions. This is known as the principle of length scale matching [7]. Energy coupling into the converter can also be improved

with an increased interfacial area between the SC and radioisotope. Lastly, the same considerations for photovoltaic performance, such as charge carrier mobility, bandgap, or recombination effects, must be examined for candidate SC materials.

The above considerations for device performance can be formalized for the total device efficiency, η :

$$\begin{aligned}\eta &\equiv \frac{P_{out}}{P_{in}} \\ &= \eta_{ec} \cdot \eta_{sc} \\ &= \eta_{ec} \left(Q \frac{q \cdot V_{oc}}{\varepsilon} FF \right),\end{aligned}\tag{3.1}$$

where η_{ec} is the energy capture efficiency, or the fraction of β -energy that is deposited in the SC converter and η_{sc} is the efficiency of the SC converter [8]. The former encompasses all geometry and energy coupling effects mentioned above, whereas the latter includes the open-circuit voltage (V_{oc}), internal quantum efficiency (IQE, Q), fill-factor (FF), and the energy required to produce a single EHP through impact ionization (ε). ε has been shown to increase linearly with converter bandgap, E_g , and is related to the upper limit of BV efficiency ($\eta_L = E_g/\varepsilon \approx E_g/(2.8E_g + 0.5)$) [4]. From this well-established relationship for the limiting efficiency, it is apparent that wide bandgap SCs result in the best performance [6].

Performance limitations in BV devices can be understood in terms of energy deposition. BVs are traditionally designed as a thick, planar SC converter with a thin film of radioisotope deposited on the surface, usually above the top contact. This limits the number of β particles which couple to the SC volume (η_{ec}) in two regards. First, β particles are emitted isotopically and, therefore, approximately 50% of all decay events will not result in any EHP generation, since half of all emitted β particles are transmitted away from the converter. Second, the top metal contact, with a high

density and stopping power, shields the converter from the majority of β particles. Both losses are compounded by the self-shielding effect of the source layer. A thick source layer is required for a high activity or power input; however, β particles will be absorbed throughout the radioisotope before being emitted out of the source volume. The shielding of the contact and source can be mitigated by using radioisotopes with high β -decay energies, but energies above approximately 100 keV will begin to cause lattice damage within the SC, significantly decreasing device lifetime [9]. Therefore, BVs tend to utilize either nickel-63 or tritium sources since their maximum β -energies are 65.9 and 18.6 keV, respectively, while their average energies are 17.4 and 5.7 keV, respectively [5]. At these energies, self-shielding and contact shielding are significant effects and, therefore, efforts have been made to create BV devices with micro- and nano-structuring to improve energy capture [10–12].

Designing BVs with NW arrays as the converting medium has been shown to be a feasible strategy for increasing η_{ec} [13]. The proposed devices, shown in Figure 3.1, are composed of a hexagonal array of axial NW p-i-n junction diodes grown on a Si substrate. Radial (core-shell) NW structures are also possible. However, it has been found that axial NWs currently out-perform radial NWs in photovoltaic applications. Therefore, axial NWs will be the focus of this study [14]. The space between the NW array is filled with the radioisotope source which can be deposited via electroplating or spin-coating, for example. The radioisotope source thickness is equal to the full height of the NWs, less 200 nm required for embedding the NWs into the top contact [15]. With this design, energy capture can be increased by up to an order of magnitude over planar devices with an equivalent power input. This large increase in η_{ec} is realized because the NW array surrounds the radioisotope, taking advantage of the

isotropic β particle emission, while the short path-length any β particle must travel to some SC converter volume significantly reduces the self-shielding effect regardless of source activity [15]. In addition, the multiple SC NWs provide β particles with multiple opportunities to deposit their energy within the converting medium as they travel through the device.

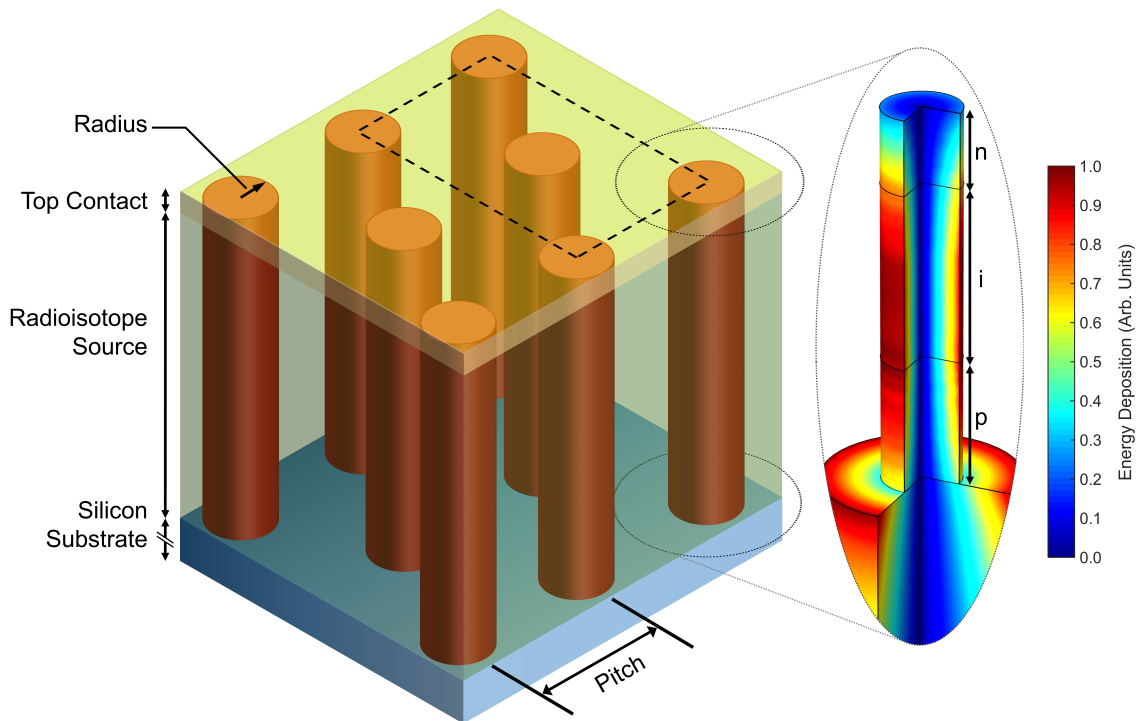


Figure 3.1: Schematic (not to scale) of a nanowire betavoltaic device, showing a portion of the hexagonal array. The dashed box outlines the non-primitive unit cell used to examine radiation interactions, while the dotted circle indicates the outline of a single nanowire unit cell used in SC charge transport simulations. The single nanowire on the right shows the various regions of the nanowire p-i-n diode, while indicating the relative energy deposition distribution within the device.

Previous work has shown that an optimum NW array diameter-to-pitch ratio exists for GaP devices which maximizes β -power capture for several source materials [16]. In the present paper, a fully coupled model is developed that also considers SC charge transport and performance for a range of candidate SCs. A fully coupled model, combining energy deposition and charge transport, allows the overall device performance and power generation to be fully optimized. This provides insight into practical BV power outputs which are attainable with NW devices for comparison with conventional planar designs. In the work discussed herein, we present an approach to fully quantify the performance of BV devices through the determination of energy capture via Monte Carlo calculations in GEANT4 and the resulting diode behaviour via drift-diffusion calculations in COMSOL Multiphysics.

3.2 Monte Carlo Simulations and Array Geometry Optimization

The first step in a fully coupled BV model is the calculation of the radiation interaction and energy capture. Monte Carlo simulations performed in the GEANT4 nuclear particle interaction toolkit [17] was used to determine both the energy capture efficiency and the spatial distribution of energy deposited throughout the NW array. This Monte Carlo modeling tallies the energy deposition within the NWs by tracking many individual β particles through a simulated volume, while calculating interaction probabilities and subsequent energy loss or scattering based on empirical datasets and material properties (density and atomic composition). The Livermore low energy dataset within GEANT4 was used [18]. Following these calculations, the spatial distribution of EHP generation rate within the NWs can be calculated and used in subsequent charge transport simulations.

The NW array was simulated by the non-primitive unit cell geometry in Figure 3.1 with periodic boundary conditions. The general approach for energy deposition calculations is equivalent to the model discussed in [16]; a volumetric source between the NWs was implemented where each β particle was initialized at a random point, with a random initial trajectory, and with an energy governed by the theoretical spectrum of the given radioactive isotope source (see Appendix A). Inelastic collisions and other interactions that transfer energy to the converter volume determine the overall energy deposition distribution function, $E_{dep}(r, z)$, with spatial coordinates r and z . With many such simulated β particles (10^7 in this work), the total power captured

by NWs, P_{cap} , is calculated (see Appendix A) as:

$$P_{cap} = 2\pi (qV_s\rho_s a) n_A \int_{r=0}^R \int_{z=0}^H E_{dep}(r, z) r dz dr, \quad (3.2)$$

where V_s , ρ_s and a are the volume, density and specific activity of the radioisotope, n_A is the NW areal number density, and q is the elementary charge. The EHP generation rate within a NW is:

$$G(r, z) = \frac{E_{dep}(r, z)}{\varepsilon} V_s \rho_s a. \quad (3.3)$$

By varying geometric parameters of the NW array, we can maximize Equation 3.2 and therefore the EHP generation and BV device performance. A qualitative depiction of this distribution in three dimensions is shown in Figure 3.1.

As shown in previous work [16], for a given combination of NW material, length, and radioisotope source, an optimum NW diameter-to-pitch ratio exists, which results in the maximum captured power, and therefore the maximum EHP generation rate. Only GaP NWs with a height of 10 μm were previously investigated [19]. Additional SCs are therefore examined herein over a wide range of NWs height. Si, gallium arsenide (GaAs), and GaP were chosen for this study due to their feasibility in NW growth as well as to provide a comparison over a range of bandgaps and surface recombination effects. The surface recombination velocity used for passivated Si, GaAs, and GaP was 10 [20], 10^3 [21], and 10^4 cm s^{-1} [22], respectively. The ionization energies (ε) for Si, GaAs, and GaP are 3.8, 4.6 and 7.8 eV, respectively [23].

Optimum diameter-to-pitch ratios have been calculated, with the resulting NW diameter maximizing the total captured power shown in Figure 3.2. For NW devices with these geometries, captured power (and therefore EHP generation rate) is greatly

increased over equivalent planar devices, as discussed below. As discussed in previous work, the captured power exhibits a maximum when examined as a function of the diameter-to-pitch ratio. This optimum ratio exists due to a trade-off between increased absorption in the NWs or decreased self-absorption (larger diameter), and a larger power input/source activity (increased pitch). To determine a physical dimension from the optimum ratio, the array geometry is constrained by setting the NW array pitch to be 100 nm greater than the NW diameter; this satisfies fabrication constraints while minimizing self-absorption in the radioisotope [16]. The radioisotope sources simulated include elemental nickel-63, tritium (at atmospheric pressure and with a density of 0.25 g cm^{-3}), as well as two compounds of nickel citrate or tritiated butyl both of which are viable choices for spin-coating fabrication methods for NW BV devices [15, 24]. The optimum diameter as a function of NW height is related to the source self-shielding effect as well as the relative differences in stopping power between the NW and source materials (see Appendix A).

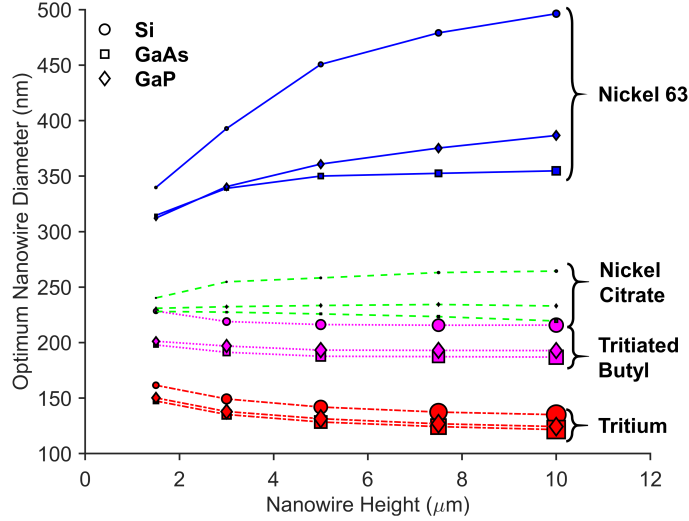


Figure 3.2: Nanowire diameter which maximizes power capture for each SC and radioisotope source across a range of nanowire height. The data markers are scaled relative to the magnitude of optimized power captured. See Appendix A for corresponding values of energy capture efficiency.

The EHP generation rate as defined in Equation 3.3 is shown in Figure 3.3 for the optimum array geometry of 3 μm long GaAs NWs with a tritium source. This design combination is used as a representative example to illustrate the energy deposition throughout the device. The total integrated captured power within the NWs and substrate for this device is 10.55 and 1.24 $\mu\text{W cm}^{-2}$, respectively (for the captured power of other device combinations, see Appendix A). As shown, the energy deposition in the substrate decays exponentially away from the source material which is similar to that seen with planar BVs [1]. However, it is clear that for NW devices, there is a strong EHP generation rate along the entire length of the NW which is expected to lead to improvements in both the collection efficiency in addition to radiation capture.

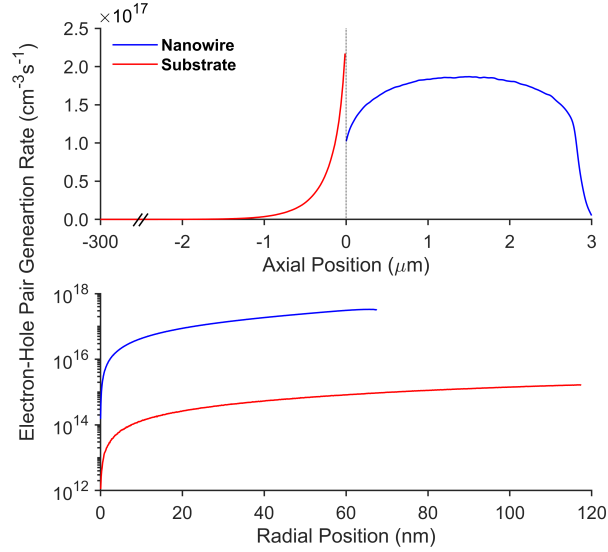


Figure 3.3: The electron-hole pair generation rate for a device composed of 3 μm long GaAs nanowires and a tritium source. The axial (top) and radial (bottom) dependence are shown separately such that integrating across either yields the total captured power (*i.e.* the axial distribution is radially averaged and the radial distribution is axially averaged). Note that for the single nanowire case shown here, the substrate is modeled with a diameter equal to the pitch of the given nanowire array. An axial and radial position of 0 corresponds to the center of the nanowire at the base where it meets the substrate.

To determine the resultant performance improvements, a comparison between the optimum NW geometry and conventional planar BVs was made. The objective function for optimization, P_{cap} , was directly compared between each design architecture. The planar cases were defined by calculating the activity present in each NW device and simulating a 1 cm² sheet of converter with a source layer thick enough to provide an equivalent activity (power input). Figure 3.4 shows this comparison for devices containing nickel-63 (see Appendix A for additional radioisotope sources). As shown, it is clear that NW devices are able to achieve large improvements in power capture

efficiency. Although the captured power for planar devices quickly saturates with increasing power input, the NW devices do not suffer from the same impacts of self-shielding. With increasing NW height, a larger radioisotope and hence power input can be deposited and, because this increased radioisotope dimension is orthogonal to the coupling direction into the NW, a saturation of power capture is not observed as seen with planar geometries. Although the radioisotope between the NWs will still absorb a fraction of the energy, the maximum thickness in the energy coupling direction is on the order of 100 nm, regardless of NW height and source thickness. The observed self-shielding is more impactful for shorter NWs or a smaller power input as well as for sources with a relatively large stopping power compared to the SC. Additionally, a fraction of β particles is emitted towards the substrate and top contact, which also contributes to a capture efficiency below 100%.

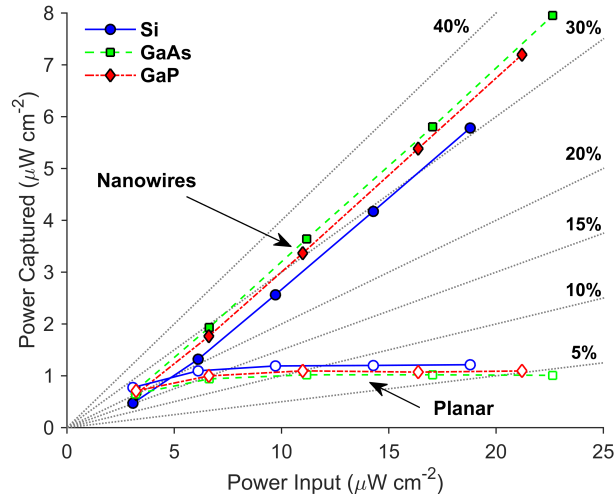


Figure 3.4: A comparison of the captured power for optimized nanowire devices using nickel-63 and corresponding planar devices with the same power input. The grey lines indicate the energy capture efficiency.

3.3 Charge Transport Modeling

With the optimum NW array geometry now defined to maximize power capture, the p-i-n junction design can be examined to fully establish device performance. The SC module in COMSOL Multiphysics was used to solve the drift-diffusion equations in a single NW model [25]. The resulting current-voltage (I-V) characteristics and maximum power point were obtained for devices with various region lengths (p, i, n) and doping levels. In the single NW model, as shown in Figure 3.1, the unit cell dimensions correspond to the pitch of the NW array, while only a fraction of the p-type Si substrate thickness (several minority carrier diffusion lengths) was modeled due to computational limitations. This provides a sufficient approximation for the charge carrier transport through the substrate [26]. The COMSOL calculations utilized the spatial distribution of the EHP generation rate from the Monte Carlo simulations as an input, and used the optimum diameter for each case as shown in Figure 3.2.

In addition to the EHP generation rate input for the COMSOL model, several material properties of the candidate SCs were used to define additional components of the drift-diffusion model. Such components included background (impurity) concentrations, trapped surface-charge densities, as well as various recombination effects. For the materials examined, trap-assisted surface and bulk recombination is defined using the Shockley-Read-Hall model, with additional components for Auger and radiative recombination [27, 28]. In addition, minority carrier mobility as a function of doping was calculated using the Arora model, accounting for both impurity and phonon scattering effects [29]. All quantities and drift-diffusion calculations used a reference temperature of 300 K. See Appendix A for the list of various material parameters used for each candidate SC.

To maximize the power output and determine the optimum diode design, the DAKOTA optimization toolkit [30] was coupled to the COMSOL model and used to tune the design variables through numerical optimization. In this approach, the NCSU DIRECT global optimization algorithm [31] was used to search the feasible design space using a coarse discretization. The output of the DIRECT optimization was used as the initial condition in a local pattern-search [32] to determine the final optimum set of design variables. The feasible design space, provided by practical limitations in NW growth, limits the range of values for the p- and n-region thicknesses and doping levels. The feasible n-region dopant concentration ranged from 1×10^{16} to $5 \times 10^{18} \text{ cm}^{-3}$, and the feasible thickness ranged from 50 to 600 nm. The feasible p-region dopant concentration ranged from 1×10^{16} to $1 \times 10^{19} \text{ cm}^{-3}$ and the feasible thickness ranged from 50 nm to the full height of the NWs, less 50 nm required for a sufficiently thick intrinsic region. A homogenous doping profile was used for all regions and the substrate dopant concentration was set to $1 \times 10^{19} \text{ cm}^{-3}$. The resulting optimum diode designs for each candidate device are given in Figure 3.5. Each design combination (NW height, NW material, and source material) utilized the corresponding optimized array diameter/pitch, as previously discussed and presented in Figure 3.2. In general, with an increasing NW length, the thicknesses of the p- and n-regions must also be increased while maintaining high doping levels. The diode performance is drift-dominated, and a larger built-in electric field dominates the improvement in open-circuit voltages [33, 34].

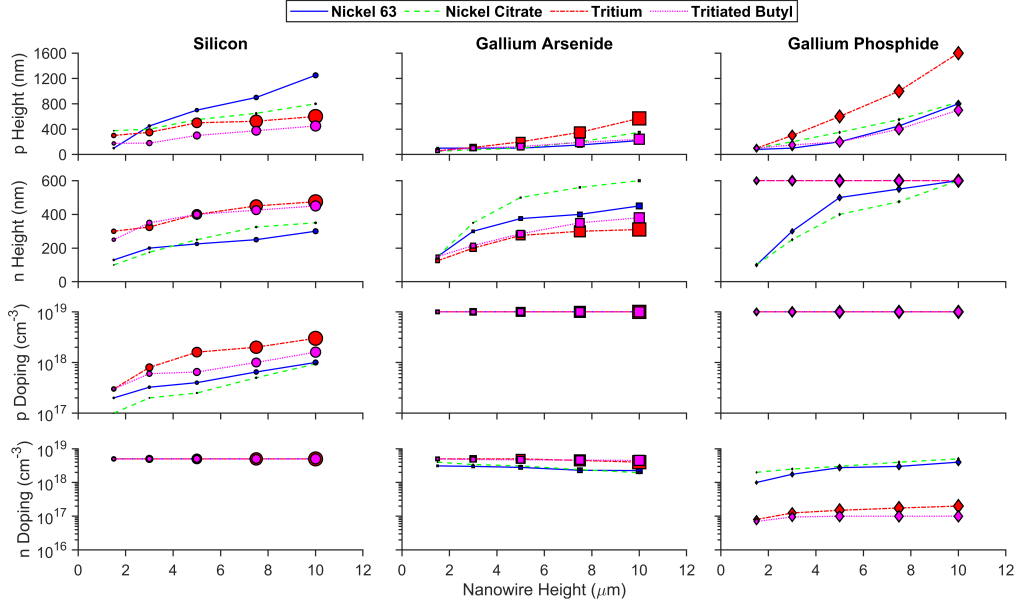


Figure 3.5: SC design variables which optimize the power output for each SC and radioisotope material combination. For a given plot, the data markers are scaled relative to the magnitude of optimized power output.

The optimum n-type segment height is, on average, less than the p-type segment height because of the relative differences in minority carrier mobility. This effect is similar to that observed in the design of solar photovoltaic cells, where carrier collection is optimized by a thick p-type base and a thin n-type emitter. Carrier collection from the undoped (i) region is favored by a large electric field, which is produced by a large doping in the n-type and p-type regions. However, for short NWs, carrier collection from the n and p regions also contribute a substantial fraction of the current due to carriers within a minority carrier diffusion length of the top and bottom of the NW. In this case, carrier collection favors low doping to minimize carrier recombination and increase the minority carrier mobility and diffusion length

(which are dopant-dependent; see Equation A.5 to Equation A.7 in Appendix A). In summary, for short NWs, a substantial built-in field can be established with lower doping while also maintaining a high mobility. Conversely, with longer NWs, the larger segment regions require additional dopants to increase the built-in electric field at the detriment of a lower mobility. We see this behaviour specifically for Si and not the III-V materials because of differences in the limits of mobility as a function of doping, and the much lower surface recombination velocity of Si compared to the III-V SCs. The high surface recombination velocity of III-V SC favors consistently high doping, regardless of NW height, to reduce surface band bending.

The diode performance (the open-circuit voltage and short-circuit current) of the optimized junction designs is shown in Figure 3.6. Here, it is shown that the open-circuit voltage of each simulated device increases with increasing bandgap, as expected. This behaviour reinforces the common practice of selecting a large bandgap material for BV designs. When examining the short-circuit current of the optimized devices, another crucial observation can be made regarding SC material selection: with increasing NW length, a saturating effect in short-circuit current is observed for GaP devices. This is due to the high surface recombination velocity of GaP which is detrimental to device IQE (shown in Appendix A). Therefore, a trade-off exists between selecting candidate SC materials which exhibit a wide bandgap and those which will not be dominated by recombination effects for devices with long NWs.

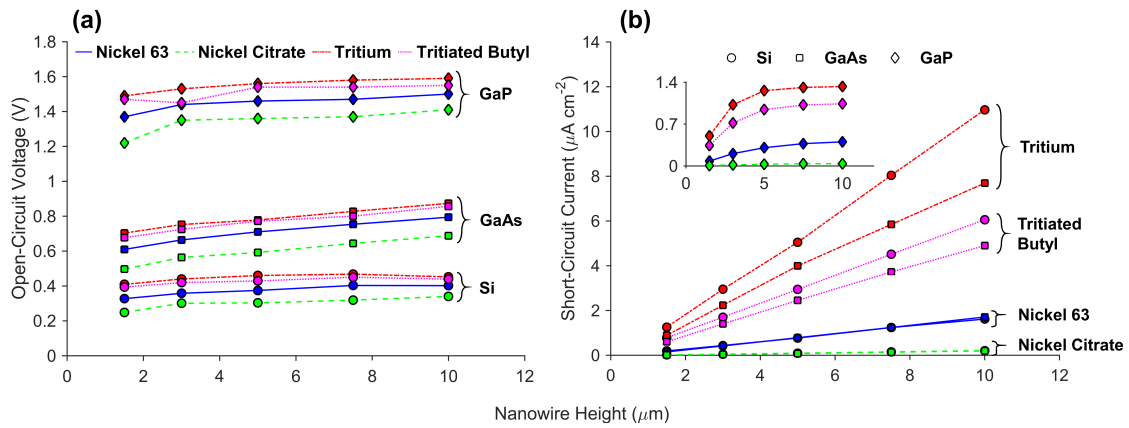


Figure 3.6: Performance of the optimized nanowire devices, showing (a) open-circuit voltage and (b) short-circuit current. The inset in (b) shows the behaviour and scale for GaP devices.

3.4 Optimized Device Performance

With the coupled BV model fully established and optimization performed on both the NW array geometry and the junction design, overall device performance can be examined. The maximum power point and BV efficiency as per Equation 3.1 is shown in Figure 3.7. Here, it is observed that modest power outputs (in excess of $1 \mu\text{W cm}^{-2}$) can be achieved for tall NWs containing tritium-based sources. In addition, and contrary to expectations, GaAs devices out-perform those made with GaP NWs. Due to the wider bandgap of GaAs compared to Si, the increased open-circuit voltage correlates to a higher power output. However, this same improvement is not seen between GaAs and GaP due to the poor surface recombination properties of the latter. With increased NW height, surface recombination begins to dominate performance, which severely limits the device current characteristics despite the increased voltage. This observation is crucial in the design of NW BVs as well as the practical assessment of limiting device efficiencies for various SC converters.

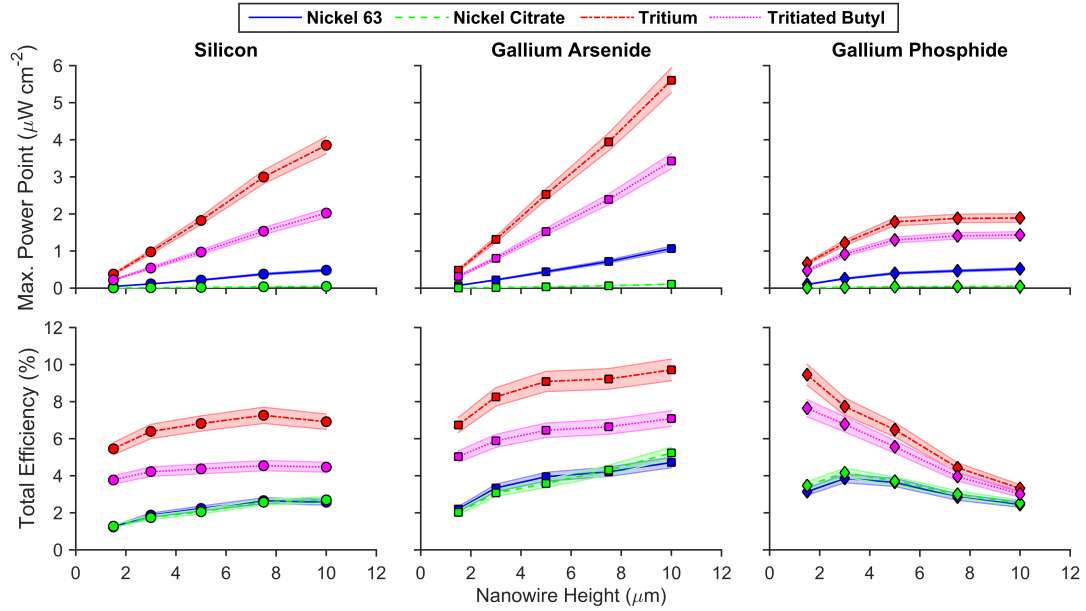


Figure 3.7: Final optimized betavoltaic performance for each SC and radioisotope material combination. The shaded regions indicate the simulation uncertainty.

As compared to the power output and total power conversion efficiency of planar designs in literature, the NW BVs exhibit large performance enhancements. Table 3.1 indicates the performance of representative devices in literature which are compared to that of the optimized NW designs in Figure 3.7. It is observed that a high-power output is achievable for the NW devices due to the ability to load high levels of activity between the tall NW structures. Therefore, additional source activity is not wasted due to excessive self-shielding as observed for planar devices with thick radioisotope layers [1].

Table 3.1: Performance of various BV devices in literature as compared to the top NW device (tritium:10 μm GaAs) simulated herein. Values omitted where not available or applicable.

Device	Power Output (nW cm^{-2})	Energy Capture Efficiency (%)	Total Efficiency (%)
Tritium:GaP [2]	-	-	4.0
Tritium:Porous Si [10, 12, 35] ¹	1.0	<44.5	0.2
Nickel-63:4H-Si [36]	100	-	6.0
Nickel-63:GaN [37]	2.7	30.5	2.7
Nickel-63:Diamond [38] ¹	3.5	<14.3	1.3
Phosphorous-33:SiC [39]	2100	12.4	4.5
Tritiated Nitroxide:4H-SiC [40] ²	-	1.5 to 48.2	<9.0
Beryllium tritide:SiC [41] ²	-	60	<10.4
Tritium:10 μm GaAs NWs	5605	72.4	9.7

¹ Experimental results which did not calculate the energy capture efficiency. The upper limit based on source activity and measured short-circuit current was inferred.

² Simulated device which does not account for complete SC physics coupling. Therefore it is expected that the total efficiency reported above is an overestimation.

Despite the exceptional performance of the NW BV designs, there still exists areas of improvement that should be investigated. In this work, only axial pin-junction NWs were assessed, which explains the poor performance of GaP devices with longer NWs. By performing similar optimizations for radial (core-shell) junction NWs, it is expected that surface recombination losses could be minimized. In addition, gradient-based dopant profiles, multijunction devices, or carrier-selective contacts may be considered for increased performance [42–44]. Therefore, an improved model which includes such additional design considerations could lead to improvements in open-circuit voltage or IQE. Although a portion of this model has been used to validate previous, unoptimized experimental results and examples from literature [15, 16], future work will also focus on the rigorous validation of the complete model through further device fabrication and testing.

3.5 Conclusions

As shown through coupled BV device modeling, NW arrays are excellent converters for simultaneously improving energy capture efficiency while achieving competitive overall performance. The model presented herein is useful for both simulating and optimizing the performance of BVs while considering the complete coupling of radiation interactions as well as SC charge transport something that has never been done for NW BV devices.

By first examining the NW array geometry, the energy capture efficiency and hence the EHP generation within the SC converters were shown to be increased by approximately an order of magnitude when compared to equivalent, planar devices. This improvement was physically explained with regards to material stopping power and the reduction in source self-shielding effects seen with the NW array architecture. The benefit of the NW devices becomes apparent when considering the addition of a thicker radioisotope (and therefore more input power); in this case, the NWs can be grown to match the source thickness and harness the added power, whereas planar devices realize a saturation in captured power due to self-shielding. Coupling these results into a SC charge-transport model allowed for the numerical optimization of junction design which provided insight into the impacts of surface recombination effects on device power output for NWs made of Si, GaAs, and GaP. Optimum pin-junction design variables were observed to provide increasing internal electric fields with increasing NW height, a trend consistent with expectations due to the drift-dominated designs.

Overall BV performance and efficiencies that are comparable or in excess of the state-of-the-art were predicted for all devices examined. Although high overall power

outputs were predicted for Si and GaAs devices (from 2 to 6 $\mu\text{W cm}^{-2}$, respectively), lower efficiencies than expected were observed for GaP NW arrays. This resulting from the large surface recombination velocity of GaP when compared to other SCs. This challenges the well-established heuristic for BV efficiency which suggests performance is maximized with an increasing converter bandgap.

In order to fully refine the model and NW devices, additional design aspects will be examined in future work. First, radial (core-shell) junction NWs can be simulated to investigate potential avenues for combating surface recombination effects for long wires. It is expected that with these structures, wider bandgap materials such as GaP or GaN could remain competitive when compared to lower bandgap SCs with well-established surface passivation techniques or naturally low recombination velocity. In addition, there remains the opportunity to investigate complex doping profiles to further improve charge collection or open-circuit voltage behaviour. Lastly, future work will focus on validating this model through device fabrication. This work has shown that NW arrays are capable of drastically improving BV performance and are a promising architecture for nuclear battery design.

References

- [1] S. T. Revankar and T. E. Adams, “Advances in Betavoltaic Power Sources,” *Journal of Energy and Power Sources*, vol. 1, no. 6, pp. 321–329, 2014.
- [2] L. C. Olsen, P. Cabaay, and B. J. Elkind, “Betavoltaic power sources,” *Physics Today*, vol. 65, no. 12, pp. 35–38, 2012.
- [3] F. K. Manasse, J. J. Pinajian, and A. N. Tse, “Schottky barrier betavoltaic battery,” *IEEE Transactions on Nuclear Science*, vol. 23, no. 1, pp. 860–870, 1976.
- [4] L. C. Olsen, “Betavoltaic energy conversion,” *Energy Conversion*, vol. 13, no. 4, pp. 117–127, 1973.
- [5] M. A. Prelas, C. L. Weaver, M. L. Watermann, E. D. Lukosi, R. J. Schott, and D. A. Wisniewski, “A review of nuclear batteries,” *Progress in Nuclear Energy*, vol. 75, no. December 2017, pp. 117–148, 2014.
- [6] T. R. Alam and M. A. Pierson, “Principles of Betavoltaic Battery Design,” *J. Energy Power Sources*, vol. 3, no. 1, pp. 11–41, 2016.
- [7] J. Dixon, A. Rajan, S. Bohlemann, D. Coso, A. D. Upadhyaya, A. Rohatgi, S. Chu, A. Majumdar, and S. Yee, “Evaluation of a Silicon 90 Sr Betavoltaic Power Source,” *Scientific Reports*, vol. 6, pp. 4–9, 2016.

- [8] A. V. Sachenko, A. I. Shkrebtii, R. M. Korkishko, V. P. Kostylyov, M. R. Kulish, and I. O. Sokolovskyi, “Efficiency analysis of betavoltaic elements,” *Solid-State Electronics*, vol. 111, pp. 147–152, 2015.
- [9] R. Bao, P. J. Brand, and D. B. Chrisey, “Betavoltaic performance of radiation-hardened high-efficiency Si space solar cells,” *IEEE Transactions on Electron Devices*, vol. 59, no. 5, pp. 1286–1294, 2012.
- [10] W. Sun, N. P. Kherani, K. D. Hirschman, L. L. Gadeken, and P. M. Fauchet, “A three-dimensional porous silicon p-n diode for betavoltaics and photovoltaics,” *Advanced Materials*, vol. 17, no. 10, pp. 1230–1233, 2005.
- [11] H. Guo and A. Lal, “Nanopower betavoltaic microbatteries,” *TRANSDUCERS 2003 - 12th International Conference on Solid-State Sensors, Actuators and Microsystems, Digest of Technical Papers*, vol. 1, pp. 36–39, 2003.
- [12] B. Liu, K. P. Chen, N. P. Kherani, and S. Zukotynski, “Power-scaling performance of a three-dimensional tritium betavoltaic diode,” *Applied Physics Letters*, vol. 95, no. 23, pp. 1–4, 2009.
- [13] N. Goktas, P. Wilson, A. Ghukasyan, D. Wagner, S. McNamee, and R. LaPierre, “Nanowires for energy: A review,” *Applied Physics Reviews*, vol. 5, no. 4, 2018.
- [14] G. Otnes and M. T. Borgström, “Towards high efficiency nanowire solar cells,” *Nano Today*, vol. 12, pp. 31–45, 2017.
- [15] S. McNamee, D. Wagner, E. Fiordaliso, D. Novog, and R. LaPierre, “GaP nanowire betavoltaic device,” *Nanotechnology*, vol. 30, no. 7, 2019.
- [16] D. Wagner, D. R. Novog, and R. R. LaPierre, “Simulation and optimization of current generation in gallium phosphide nanowire betavoltaic devices,” *Journal of Applied Physics*, vol. 125, no. 16, 2019.

- [17] S. Agostinelli *et al.*, “GEANT4 – a simulation toolkit,” *Nuclear Instruments and Methods in Physics Research Section A: Accelerators, Spectrometers, Detectors and Associated Equipment*, vol. 506, no. 3, pp. 250–303, 2003.
- [18] T. Toshito *et al.*, “Validation of New Geant4 Electromagnetic Physics Models for Ion Therapy Applications,” *Progress in Nuclear Science and Technology*, vol. 2, no. 0, pp. 918–922, 2011.
- [19] D. Wagner, D. R. Novog, and R. R. LaPierre, “Design and Optimization of Nanowire Betavoltaic Generators,” *Journal of Applied Physics*, vol. 128, no. 1, 2020.
- [20] T. Lauinger, J. Schmidt, A. G. Aberle, and R. Hezel, “Record low surface recombination velocities on 1 cm p-silicon using remote plasma silicon nitride passivation,” *Applied Physics Letters*, vol. 68, no. 9, pp. 1232–1234, 1996.
- [21] A. K. J.M. Olson, R.K., Ahrenkiel, D.J. Dunlavy, Brian Keyes, “Ultralow recombination velocity at Ga_{0.5}In_{0.5}P/GaAs Heterointerfaces,” *Applied Physics Letters*, vol. 1208, no. December 1998, pp. 10–13, 1989.
- [22] X. Lu, R. Hao, M. Diaz, R. L. Opila, and A. Barnett, “Improving GaP solar cell performance by passivating the surface using Al_xGa_{1-x}P epi-layer,” *IEEE Journal of the Electron Devices Society*, vol. 1, no. 5, pp. 111–116, 2013.
- [23] C. A. Klein, “Bandgap dependence and related features of radiation ionization energies in semiconductors,” *Journal of Applied Physics*, vol. 39, no. 4, pp. 2029–2038, 1968.
- [24] P. E. Sims, L. C. Dinetta, and A. M. Barnett, “High efficiency GaP power conversion for betavoltaic Applications,” *NASA. Lewis Research Center, Proceedings of the 13th Space Photovoltaic Research and Technology Conference*, vol. 13,

- pp. 373–382, 1994.
- [25] COMSOL Multiphysics, “Semiconductor Module User’s Guide,” 2018.
- [26] A. H. Trojnar, C. E. Valdivia, R. R. LaPierre, K. Hinzer, and J. J. Krich, “Optimizations of GaAs Nanowire Solar Cells,” *IEEE Journal of Photovoltaics*, vol. 6, no. 6, pp. 1494–1501, 2016.
- [27] R. Hall, “Electron-Hole Recombination in Silicon,” *Physical Review*, vol. 87, no. 2, p. 387, 1952.
- [28] W. Shockley and W. T. Read, “Statistics of the recombinations of holes and electrons,” *Physical Review*, vol. 87, no. 5, pp. 835–842, 1952.
- [29] N. D. Arora, J. R. Hauser, and D. J. Roulston, “Electron and Hole Mobilities in Silicon as a Function of Concentration and Temperature,” *IEEE Transactions on Electron Devices*, vol. 29, no. 2, pp. 292–295, 1982.
- [30] T. Trucano *et al.*, “Dakota, A Multilevel Parallel Object-Oriented Framework for Design Optimization, Parameter Estimation, Uncertainty Quantification, and Sensitivity Analysis,” tech. rep., Sandia National Laboratories, 2014.
- [31] J. Gablonksy, “DIRECT Version 2.0 User Guide Technical Report,” 2001.
- [32] G. A. Gray and T. G. Kolda, “Algorithm 856: APPSPACK 4.0: Asynchronous parallel pattern search for derivative-free optimization,” *ACM Transactions on Mathematical Software*, vol. 32, no. 3, pp. 485–507, 2006.
- [33] H. Okamoto, T. Yamaguchi, S. Nonomura, and Y. Hamakawa, “DRIFT TYPE PHOTOVOLTAIC EFFECT IN a-Si p-i-n JUNCTION,” *Le Journal de Physique Colloques*, vol. 42, no. C4, pp. C4–507–C4–510, 1981.
- [34] A. W. Welch, L. L. Baranowski, H. Peng, H. Hempel, R. Eichberger, T. Unold, S. Lany, C. Wolden, and A. Zakutayev, “Trade-Offs in Thin Film Solar Cells

- with Layered Chalcostibite Photovoltaic Absorbers,” *Advanced Energy Materials*, vol. 7, no. 11, 2017.
- [35] J. P. Clarkson, W. Sun, K. D. Hirschman, L. L. Gadeken, and P. M. Fauchet, “Betavoltaic and photovoltaic energy conversion in three-dimensional macroporous silicon diodes,” *Physica Status Solidi (A) Applications and Materials Science*, vol. 204, no. 5, pp. 1536–1540, 2007.
- [36] A. L. M.V.S. Chandrashekar, Christopher I. Thomas, Hui Li, M.G. Spencer, “Demonstration of a 4H SiC betavoltaic cell,” *Applied Physics Letters*, vol. 88, 2006.
- [37] Z. Cheng, H. San, Z. Feng, B. Liu, and X. Chen, “High open-circuit voltage betavoltaic cell based on GaN pin homojunction,” *Electronics Letters*, vol. 47, no. 12, p. 720, 2011.
- [38] V. S. Bormashov, S. Y. Troschiev, S. A. Tarelkin, A. P. Volkov, D. V. Teteruk, A. V. Golovanov, M. S. Kuznetsov, N. V. Kornilov, S. A. Terentiev, and V. D. Blank, “High power density nuclear battery prototype based on diamond Schottky diodes,” *Diamond and Related Materials*, vol. 84, no. February, pp. 41–47, 2018.
- [39] C. J. Eiting, V. Krishnamoorthy, S. Rodgers, T. George, J. D. Robertson, and J. Brockman, “Demonstration of a radiation resistant, high efficiency SiC betavoltaic,” *Applied Physics Letters*, vol. 88, no. 6, 2006.
- [40] J. Russo, M. S. Litz, I. I. William Ray, H. Berk, H. Cho, D. I. Bigio, A. Wertz, and T. R. Alam, “Planar and textured surface optimization for a tritium-based betavoltaic nuclear battery,” *International Journal of Energy Research*, vol. 43, no. 9, pp. 4370–4389, 2019.

- [41] T. R. Alam, M. G. Spencer, M. A. Prelas, and M. A. Pierson, “Design and optimization of radioisotope sources for betavoltaic batteries,” *International Journal of Energy Research*, vol. 42, no. 7, pp. 2564–2573, 2018.
- [42] N. Anttu, “Physics and design for 20% and 25% efficiency nanowire array solar cells,” *Nanotechnology*, vol. 30, no. 7, 2019.
- [43] V. Raj, L. Fu, H. H. Tan, and C. Jagadish, “Design Principles for Fabrication of InP-Based Radial Junction Nanowire Solar Cells Using an Electron Selective Contact,” *IEEE Journal of Photovoltaics*, vol. 9, no. 4, pp. 980–991, 2019.
- [44] Y. Wang, Y. Zhang, D. Zhang, S. He, and X. Li, “Design High-Efficiency III-V Nanowire/Si Two-Junction Solar Cell,” *Nanoscale Research Letters*, vol. 10, no. 1, pp. 0–4, 2015.

Chapter 4

Core-shell Structures

Core-shell p-i-n junctions are investigated to extend the results presented in Chapter 3 and examine an approach to surpass the limitations of axial junction devices. By implementing core-shell junctions, it is predicted that the losses due to surface recombination will be reduced and the resulting SC efficiency will be improved. The devices presented in this chapter represent the highest performance possible given the current architecture and material choice and thus, will provide a benchmark for NW BVs moving forward.

The results indicate that core-shell junctions do in fact have increased performance over the devices presented in Chapter 3. Additionally, it is predicted that the performance of core-shell devices closely approach the ideal limit determined specifically for NW BVs.

Genetic Algorithm Optimization of Core-Shell Nanowire Betavoltaic Generators

DOI: TBD (Submitted: May, 2020. Currently under review)

Reproduced from:

D. Wagner, D. R. Novog, and R. R. LaPierre, “Genetic Algorithm Optimization of Core-Shell Nanowire Betavoltaic Generators,” *Nanotechnology*, Submitted, 2020.

...with the permission of IOP Publishing

ABSTRACT: Numerical optimization has been used to determine the optimum junction design for core-shell nanowires used in betavoltaic generators. A genetic algorithm has been used to calculate the relative thickness, height, and doping of each segment within silicon, gallium arsenide, and gallium phosphide nanowires. Using the simulated spectra and energy deposition of nickel-63, nickel citrate, tritium, and tritiated butyl, devices with power output and overall efficiency up to $8 \mu\text{W cm}^{-2}$ and 12%, respectively, have been predicted. Compared to previously investigated axial nanowires, the core-shell structures simulated here have realized drastic improvements by reducing surface recombination for longer nanowires. In addition, core-shell nanowires are shown to be capable of nearly matching the ideal performance predicted for this device structure. A new approach for calculating the practical upper limit of betavoltaic performance is presented and additional methods for improvement are discussed.

4.1 Introduction

BV generators convert the kinetic energy of β -particles into electrical energy within a SC, analogous to the photovoltaic effect in solar cells. The output of such devices will persist for a duration on the order of the half-life of the radioisotope source, making BVs a long-lasting power supply that is insensitive to environmental conditions [1]. However, the rate of β decay and the resulting particle flux is limited. This results in a device power output on the order of nano/microwatts [2]. Applications that benefit from BVs include remote sensors, biomedical implants, or space probes [3].

The total efficiency, η_{tot} , of a BV device can be defined as the product of the energy capture efficiency, η_{ec} , and the SC conversion efficiency, η_{sc} [4]. The former describes the fraction of β energy that is deposited in the SC whereas the latter is given by:

$$\eta_{sc} = \frac{q \cdot FF \cdot V_{oc} \cdot Q}{\varepsilon}, \quad (4.1)$$

where q is the elementary charge, FF is the fill-factor, V_{oc} is the open-circuit voltage, Q is the internal quantum efficiency, and ε is the average energy required to produce an electron-hole pair in the SC material. For an ideal device, Equation 4.1 approaches the ratio of the SC bandgap, E_g , to ε [4]. However, this assumes that the β -generated current is large enough such that V_{oc} approaches E_g/q .

4.1.1 Energy Capture of Nanowire Arrays

Recent work has examined nanostructuring to maximize η_{ec} . The shielding of β energy within the radioisotope source has been minimized and BV device performance has been improved [5–7]. We have shown that a hexagonal NW array with a radioisotope source deposited between the NWs is an effective form of nanostructuring for increasing η_{ec} [8]. Previous work [9] used Monte Carlo simulations in GEANT4 [10] to optimize the NW array geometry (diameter and pitch) for maximum power capture. This was done across a range of NW lengths for Si, GaAs, and GaP, all well established materials for NW growth. Common BV sources (^{63}Ni and ^3H /tritium) as well as those viable for spin-coating deposition [11] (^{63}Ni -citrate or tritiated butyl) were considered. Source material properties are given in Appendix B.

NW arrays are an attractive medium for BV devices as they are able to overcome the fundamental limitation of self-shielding inherent in a planar SC geometry. Self-shielding occurs when additional source volume is loaded onto the device in an effort to increase power output; although power input is increased, the relative number of β -particles shielded by the source also increases. Ultimately, this results in a saturation of the device power output as the radioisotope layer thickness increases [12]. Moreover, this implies that η_{ec} approaches zero with increasing power input for a planar SC geometry. As shown by the optimized energy capture for various NW device designs in Figure 4.1, this is not the case for NW BV devices. For the results of Figure 4.1, the array geometry was optimized as previously reported in [8].

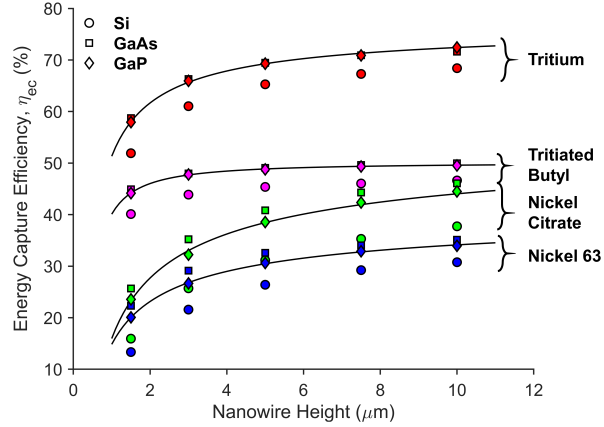


Figure 4.1: Optimized energy capture of nanowire arrays. Power law fits are shown for GaP devices to guide the eye.

As shown in Figure 4.1, η_{ec} for the NW devices continues to increase with NW height, H , because the β -source thickness between the NWs is relatively constant regardless of the NW/source height (*i.e.* the self-shielding is limited) [9]. Therefore, by growing longer NWs and increasing the source loading in the device, the power output continues to increase and the source efficiency saturates to a non-zero value. This behaviour was fit to an inverse power law equation in the form of $\eta_{ec}(H) = a/b^H + c$ using a subspace trust-region method [13] (illustrated for GaP in Figure 4.1 with remaining fits in Appendix B). By assuming infinitely long NWs ($H \rightarrow \infty$), this allows us to extract the best-case capture efficiency for each design combination (given in Table 4.1). It is clear from this behaviour that, unlike conventional planar BV devices, the effects of self-shielding do not diminish overall performance and the captured power in final devices is unbounded with increasing NW length and power input. The performance of infinitely long NWs is almost reached for a NW length of only 10 μm , as seen in Figure 4.1.

Table 4.1: Best-case energy capture for NWs with $H \rightarrow \infty$.

SC	Source	$\lim_{H \rightarrow \infty} \eta_{ec}$ (%)
Silicon	^{63}Ni	37.23
	$^{63}\text{Ni-Cit}$	52.42
	^3H	71.53
	Trit-Butyl	47.62
Gallium Arsenide	^{63}Ni	38.64
	$^{63}\text{Ni-Cit}$	56.12
	^3H	73.23
Gallium Phosphide	Trit-Butyl	50.60
	^{63}Ni	42.77
	$^{63}\text{Ni-Cit}$	58.82
	^3H	77.12
	Trit-Butyl	50.10

4.2 Methods

The radiation capture of the optimum NW arrays has been coupled to SC charge transport calculations in the COMSOL Multiphysics toolkit [14]. This approach optimized the design of axial p-i-n junction NWs, for a given diameter and pitch, to maximize η_{sc} [9]. However, it has been shown that for these axial junctions, longer NWs begin to suffer due to surface recombination effects (a reduced Q and V_{oc} in Equation 4.1). This is especially the case for the wider bandgap SC,GaP, considered here. Overall, despite the improvements in energy capture that NW arrays provide, surface recombination remains a key limitation in the device design. Therefore, the present paper considers core-shell p-i-n junction designs to mitigate surface recombination and further improve device performance [15]. The structure of a single NW in such a design is shown in Figure 4.2.

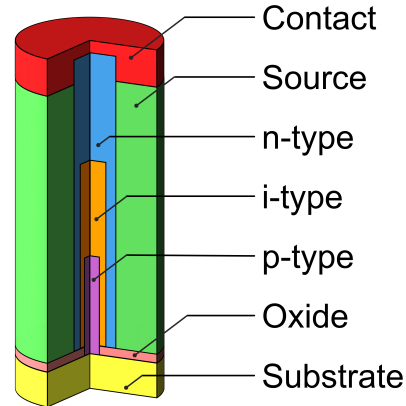


Figure 4.2: A single nanowire representation of a core-shell BV device.

Here, the design variables of the junction are the height and radius of the p-type core, the height of the n-type cap, the thickness of the n-type shell, and the respective dopant concentrations. The length and thickness of the intrinsic (unintentionally doped) shell are determined by default as the remainder of the NW. The overall diameter for a given combination of SC, source, and NW height, is held constant according to the optimum array geometry defined in previous work [9]. The n-type portion is embedded 200 nm into the top-contact and the p-type silicon substrate extends 300 μm to the back contact of the device. A 30 nm thick silicon oxide layer, hexagonally patterned with 100 nm holes, prevents the shell of the NWs from shorting the device while providing a current path between the substrate and NW core.

The previous axial p-i-n junctions [9] were numerically optimized using a direction-based search algorithm [16]. This approach sufficed when only the individual p- and n-type lengths were varied. However, for larger design-space problems, this approach is too computationally intensive [17]. Therefore, a single-objective genetic algorithm [18] in the DAKOTA toolkit [19] was employed for the core-shell structures examined here. With the exception of the optimization routine and the diode structure, the model presented here is identical to previous work [8]. This includes the energy deposition and electron-hole pair generation rate for the optimum NW diameter and array pitch, as well as components of the drift-diffusion model (recombination and transport properties).

Each design variable was constrained to remain practical for fabrication. The genetic algorithm enforced a minimum segment dimension of 10 nm in both radial and axial directions. The upper bound for each segment was determined by the total NW height or optimum NW diameter for a given design (less the lower limit for the other two segments). In addition, the n- and p-type dopant concentrations were limited to 5×10^{18} and $1 \times 10^{19} \text{ cm}^{-3}$, respectively, both with a lower bound of $1 \times 10^{16} \text{ cm}^{-3}$. The intrinsic region was assumed to have an unintentional doping of $1 \times 10^{15} \text{ cm}^{-3}$ for all SCs. These doping ranges represent the practical limitations of self-assisted vapour-liquid-solid growth of NWs via molecular beam epitaxy [20].

The generation size for the genetic algorithm was 100 samples. The initial generation was set to the 64 simplex points of the design space plus 36 random points. This initialization ensured that the extremities of the design space would be explored. Convergence was met when the average power output for an entire population changed no less than 1% over the previous 10 generations.

4.3 Results & Discussion

4.3.1 Optimized Designs

The optimized junction designs are given in Figure 4.3. Not shown are the dopant concentrations for each design, as the optimum values were constant across all devices for a given SC. The optimum n-type doping was determined to be $5 \times 10^{18} \text{ cm}^{-3}$ for all cases while the optimum p-type doping was 1×10^{19} and $1 \times 10^{16} \text{ cm}^{-3}$ for III-V NWs and Si, respectively.

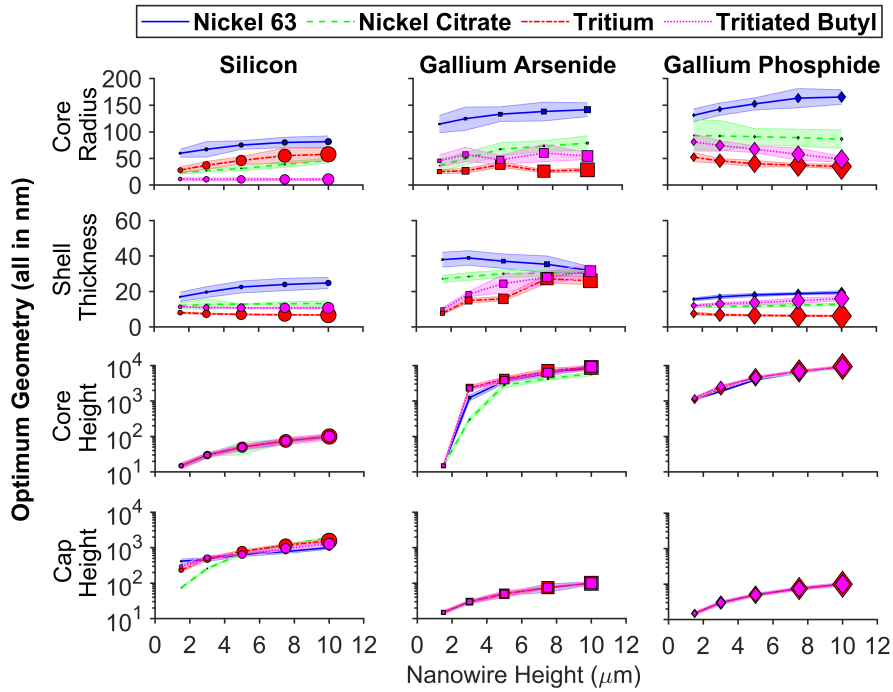


Figure 4.3: Optimum junction designs. Markers are scaled relative to the power output for the corresponding design. The shaded region indicates the 95% confidence interval.

Optimum performance for the core-shell designs is given in Figure 4.4, which shows the output power, P_{out} , the total simulated efficiency, $\eta_{tot} = P_{out}/P_{in}$, and the improvement over axial structures. The power input, P_{in} , used for each design is a function of source volume and provided in Appendix B. Efficiencies are competitive with the highest performance BVs described in literature, [5, 12, 21] with $\eta_{tot} > 10\%$ predicted for lower density source (tritium-based) designs. Additionally, as expected, the overall power output increases linearly with NW height. Although all design combinations realize an improvement over the axial junctions, this factor is only on the order of 1 to 1.5 for Si and GaAs. On the other hand, the improvement was significant for GaP, which suffered the most from surface recombination. Therefore, because η_{ec} is only dependent on array geometry and is constant for both axial and core-shell designs, it is clear that the improvements are due entirely to an increase in η_{sc} . This improvement in η_{sc} indicates that core-shell structures are effective at reducing recombination losses in long NWs.

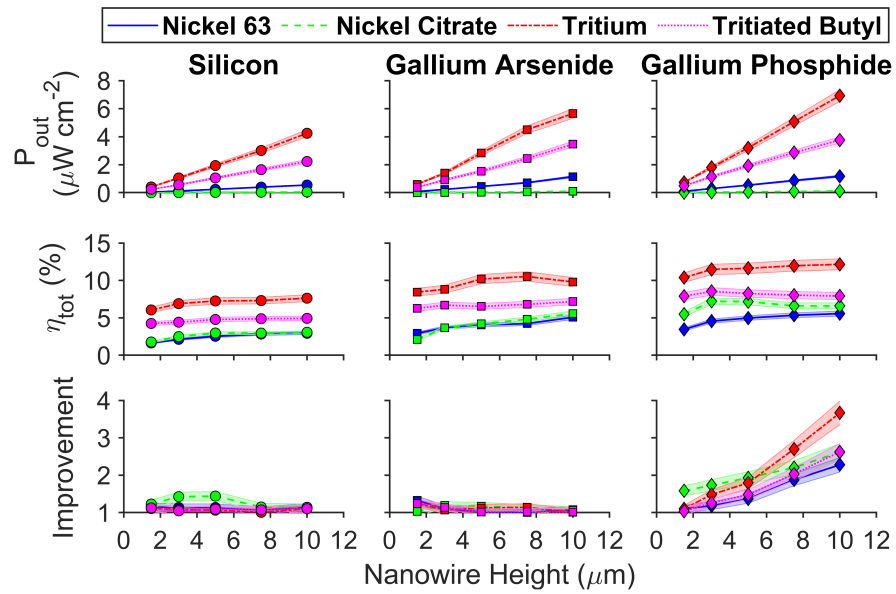


Figure 4.4: Performance of optimum designs (power output, P_{out} and total efficiency, η_{tot}) and comparison to axial NWs in previous work. The shaded region indicates the overall simulation uncertainty.

4.3.2 Best-Case Device Performance

Now that the NW BV devices have been optimized within practical fabrication limits, it would be useful to quantify their performance relative to the best-case device efficiencies possible. As mentioned earlier, the limiting BV efficiency is:

$$\eta_{lim} = \frac{E_g}{\varepsilon} \quad (4.2)$$

and is listed in Table 4.2. Values of ε for Si, GaAs, and GaP, were (3.8 ± 0.01) , (4.6 ± 0.06) , and (7.8 ± 0.8) eV, respectively [22,23]. However, η_{lim} is not a practical quantity. As mentioned previously, the limiting efficiency assumes that $qV_{oc} = E_g$. This is often not achievable for BVs where the short-circuit current, J_{sc} , is on the order of nA cm^{-2} to $\mu\text{A cm}^{-2}$. The limiting BV efficiency also assumes $\eta_{ec} = 100\%$ which is impractical due to the non-zero energy loss in any finite volume of source material [24]. However, high-performance NWs have been shown to achieve a fill-factor and internal quantum efficiency close to unity and therefore this assumption will hold [25,26]. Therefore, the best-case device efficiency, η_{∞} , for the NW BVs presented here will be calculated with the upper bound for η_{ec} , as given in Table 4.1, as well as V_{oc} as calculated below. See Appendix B for details on this method. With these assumptions, the best-case NW device efficiency is:

$$\eta_{\infty} = \left(0.99 \cdot \lim_{H \rightarrow \infty} \eta_{ec}\right) \left(\frac{q \cdot V_{oc}}{\varepsilon}\right). \quad (4.3)$$

As per the well-known solar cell equation, [4] V_{oc} can be calculated as:

$$V_{oc} = \frac{kT}{q} \ln \left(\frac{J_{sc}}{J_0} + 1\right), \quad (4.4)$$

where J_0 is the reverse saturation current density of the diode and kT/q is the thermal voltage, 0.026 eV. In order to constrain the device to a finite size, the best-case J_{sc} is calculated for NWs that achieve 99% the value of η_{ec} given in Table 4.1. Using the carrier transport properties from previous work [9], J_0 for each SC is calculated from:

$$J_0 = q \cdot n_i^2 \left(\frac{1}{N_D} \sqrt{\frac{D_p}{\tau_p}} + \frac{1}{N_A} \sqrt{\frac{D_n}{\tau_n}} \right), \quad (4.5)$$

where n_i is the intrinsic carrier concentration and N_D and N_A are the donor and acceptor concentrations, respectively. Additionally, D_p and D_n are the diffusion coefficients of holes and electrons, respectively, and τ_p and τ_n are the minority carrier lifetimes of the holes and electrons, respectively – all of which vary with dopant concentration [27]. A simplex search method was used to optimize dopant concentrations for a minimum J_0 (given in Appendix B). The dopant concentrations are limited to the same ranges as in the genetic algorithm by using a sine variable transform [28].

Table 4.2 compares η_{tot} for the 10 μm NWs given in Figure 4.4, the results of Equation 4.3, as well as the limiting BV efficiency (Equation 4.2) for a given SC. All trends in η_∞ are as expected. For example, an increased device performance is seen for SCs with a wider bandgap due to the increased V_{oc} . Additionally, because tritium-based sources have a lower mass density compared to nickel-based sources, the resulting value of η_{ec} is also higher, and η_{tot} is nearly equal to η_∞ . This also provides insight to the large discrepancy between η_∞ and η_{lim} . Although NW BVs exhibit a drastic improvement in η_{ec} compared to the planar SC geometry, the non-zero loss due to absorption in the source impacts performance. For devices with ^{63}Ni , $^{63}\text{Ni-Cit}$, ^3H , and Trit-Butyl, the average factor of reduction in η_{ec} from unity is 2.54, 1.80, 1.35, and 2.02, respectively. The performance of the tritium-based devices highlights

the importance of engineering the source material for maximum activity density and minimum self-absorption. The discrepancy between η_∞ and η_{lim} is also caused by limitations in J_{sc} , which prevent BVs from achieving high values of V_{oc} . For NWs made of Si, GaAs, and GaP, the average factor of reduction in η_{sc} from unity is 2.02, 1.57, and 1.34, respectively. In order to increase V_{oc} further, a β -generated current would need to be orders of magnitude higher than those presented in this work, which is infeasible for practical β sources.

Table 4.2: Comparison of optimum device efficiencies. All values of η_{tot} exhibit a relative uncertainty of 6%.

SC	Source	η_{tot} (%)	η_∞ (%)	η_{lim} (%)
Silicon	^{63}Ni	2.94	5.70 ± 0.38	29.47 ± 0.08
	$^{63}\text{Ni-Cit}$	3.07	7.54 ± 0.38	
	^3H	7.62	10.41 ± 0.03	
	Trit-Butyl	4.93	6.48 ± 0.02	
Gallium Arsenide	^{63}Ni	5.08	7.59 ± 0.10	30.96 ± 0.40
	$^{63}\text{Ni-Cit}$	5.57	11.10 ± 0.17	
	^3H	10.53	14.22 ± 0.19	
	Trit-Butyl	7.18	9.52 ± 0.12	
Gallium Phosphide	^{63}Ni	5.57	9.47 ± 0.99	28.97 ± 2.97
	$^{63}\text{Ni-Cit}$	7.21	12.83 ± 1.34	
	^3H	12.16	16.60 ± 1.72	
	Trit-Butyl	8.53	10.28 ± 1.07	

Although they approach the best-case NW efficiencies, the designs presented herein could be improved upon. Rigorous optimization of the materials for the radioisotope should be investigated. Much work has been done on synthesizing compounds that minimize source self-shielding [12, 29, 30] and, when coupled with the geometry of the NW arrays, could lead to further increases in η_{ec} . Future work will additionally focus on validating the model for BV performance and the associated optimization through device fabrication and testing.

4.4 Conclusion

In conclusion, we have predicted that high-performance BV generators are achievable with NW arrays. In addition to the high potential energy capture efficiency, the higher quality NW diodes offered by core-shell structures allow for increased SC conversion efficiency. Core-shell structures are able to reduce the impact of recombination in longer NWs, making wider bandgap devices feasible. Nearly all device combinations achieve a predicted total power output in excess of $1 \mu\text{W cm}^{-2}$ and the total device efficiency of tritium-based designs are capable of surpassing 10%. By specifically examining quantities such as the reverse saturation current, maximum achievable energy capture efficiency, and open-circuit voltage, we have also shown that the core-shell NW BVs simulated here approach the best-case device performances. Overall, we have shown that NW BVs exhibit impressive efficiency as well as output power and are therefore a feasible architecture for producing devices with near ideal performance.

References

- [1] L. C. Olsen, P. Cabaay, and B. J. Elkind, “Betavoltaic power sources,” *Physics Today*, vol. 65, no. 12, pp. 35–38, 2012.
- [2] T. R. Alam and M. A. Pierson, “Principles of Betavoltaic Battery Design,” *J. Energy Power Sources*, vol. 3, no. 1, pp. 11–41, 2016.
- [3] M. A. Prelas, C. L. Weaver, M. L. Watermann, E. D. Lukosi, R. J. Schott, and D. A. Wisniewski, “A review of nuclear batteries,” *Progress in Nuclear Energy*, vol. 75, no. December 2017, pp. 117–148, 2014.
- [4] A. V. Sachenko, A. I. Shkrebtii, R. M. Korkishko, V. P. Kostylyov, M. R. Kulish, and I. O. Sokolovskyi, “Efficiency analysis of betavoltaic elements,” *Solid-State Electronics*, vol. 111, pp. 147–152, 2015.
- [5] J. Russo, M. S. Litz, I. I. William Ray, H. Berk, H. Cho, D. I. Bigio, A. Wertz, and T. R. Alam, “Planar and textured surface optimization for a tritium-based betavoltaic nuclear battery,” *International Journal of Energy Research*, vol. 43, no. 9, pp. 4370–4389, 2019.
- [6] B. Liu, K. P. Chen, N. P. Kherani, and S. Zukotynski, “Power-scaling performance of a three-dimensional tritium betavoltaic diode,” *Applied Physics Letters*, vol. 95, no. 23, pp. 1–4, 2009.

- [7] M. Mohamadian, S. Fegghi, and H. Afariadeh, “Geometrical Optimization of GaN Betavoltaic Microbattery,” *Proceedings of the 7th WSEAS International Conference on Power Systems*, pp. 247–250, 2007.
- [8] D. Wagner, D. R. Novog, and R. R. LaPierre, “Simulation and optimization of current generation in gallium phosphide nanowire betavoltaic devices,” *Journal of Applied Physics*, vol. 125, no. 16, 2019.
- [9] D. Wagner, D. R. Novog, and R. R. LaPierre, “Design and Optimization of Nanowire Betavoltaic Generators,” *Journal of Applied Physics*, vol. 128, no. 1, 2020.
- [10] S. Agostinelli *et al.*, “GEANT4 – a simulation toolkit,” *Nuclear Instruments and Methods in Physics Research Section A: Accelerators, Spectrometers, Detectors and Associated Equipment*, vol. 506, no. 3, pp. 250–303, 2003.
- [11] S. McNamee, D. Wagner, E. Fiordaliso, D. Novog, and R. LaPierre, “GaP nanowire betavoltaic device,” *Nanotechnology*, vol. 30, no. 7, 2019.
- [12] T. R. Alam, M. G. Spencer, M. A. Prelas, and M. A. Pierson, “Design and optimization of radioisotope sources for betavoltaic batteries,” *International Journal of Energy Research*, vol. 42, no. 7, pp. 2564–2573, 2018.
- [13] T. F. Coleman and Y. Li, “An interior trust region approach for nonlinear minimization subject to bounds,” *SIAM Journal on optimization*, vol. 6, no. 2, pp. 418–445, 1996.
- [14] COMSOL Multiphysics, “Semiconductor Module User’s Guide,” 2018.
- [15] G. Otnes and M. T. Borgström, “Towards high efficiency nanowire solar cells,” *Nano Today*, vol. 12, pp. 31–45, 2017.
- [16] J. Gablonksy, “DIRECT Version 2.0 User Guide Technical Report,” 2001.

- [17] J. C. Meza, R. S. Judson, T. R. Faulkner, and A. M. Treasurywala, “A comparison of a direct search method and a genetic algorithm for conformational searching,” *Journal of Computational Chemistry*, vol. 17, no. 9, pp. 1142–1151, 1996.
- [18] J. Eddy and K. Lewis, “Effective generation of Pareto sets using genetic programming,” *Proceedings of the ASME Design Engineering Technical Conference*, vol. 2, no. 1, pp. 783–791, 2001.
- [19] T. Trucano *et al.*, “Dakota, A Multilevel Parallel Object-Oriented Framework for Design Optimization, Parameter Estimation, Uncertainty Quantification, and Sensitivity Analysis,” tech. rep., Sandia National Laboratories, 2014.
- [20] N. I. Goktas, E. M. Fiordaliso, and R. R. LaPierre, “Doping assessment in GaAs nanowires,” *Nanotechnology*, vol. 29, no. 23, 2018.
- [21] S. I. Maximenko, J. E. Moore, C. A. Affouda, and P. P. Jenkins, “Optimal Semiconductors for 3H and 63Ni Betavoltaics,” *Scientific Reports*, vol. 9, no. 1, pp. 1–8, 2019.
- [22] G. Bertuccio and D. Maiocchi, “Electron-hole pair generation energy in gallium arsenide by x and γ photons,” *Journal of Applied Physics*, vol. 92, no. 3, pp. 1248–1255, 2002.
- [23] C. A. Klein, “Bandgap dependence and related features of radiation ionization energies in semiconductors,” *Journal of Applied Physics*, vol. 39, no. 4, pp. 2029–2038, 1968.
- [24] G. Gui, K. Zhang, J. P. Blanchard, and Z. Ma, “Prediction of 4H-SiC betavoltaic microbattery characteristics based on practical Ni-63 sources,” *Applied Radiation and Isotopes*, vol. 107, pp. 272–277, 2016.

- [25] R. R. LaPierre, A. C. Chia, S. J. Gibson, C. M. Haapamaki, J. Boulanger, R. Yee, P. Kuyanov, J. Zhang, N. Tajik, N. Jewell, and K. M. Rahman, “III-V nanowire photovoltaics: Review of design for high efficiency,” *Physica Status Solidi - Rapid Research Letters*, vol. 7, no. 10, pp. 815–830, 2013.
- [26] V. Raj, L. Fu, H. H. Tan, and C. Jagadish, “Design Principles for Fabrication of InP-Based Radial Junction Nanowire Solar Cells Using an Electron Selective Contact,” *IEEE Journal of Photovoltaics*, vol. 9, no. 4, pp. 980–991, 2019.
- [27] N. D. Arora, J. R. Hauser, and D. J. Roulston, “Electron and Hole Mobilities in Silicon as a Function of Concentration and Temperature,” *IEEE Transactions on Electron Devices*, vol. 29, no. 2, pp. 292–295, 1982.
- [28] G. R. Atwood and W. W. Foster, “Transformation of Bounded Variables in Simplex Optimization Techniques,” *Industrial and Engineering Chemistry Process Design and Development*, vol. 12, no. 4, pp. 485–486, 1973.
- [29] J. Russo, M. Litz, W. Ray, G. M. Rosen, D. I. Bigio, and R. Fazio, “Development of tritiated nitroxide for nuclear battery,” *Applied Radiation and Isotopes*, vol. 125, no. March, pp. 66–73, 2017.
- [30] C. Thomas, S. Portnoff, and M. G. Spencer, “High efficiency 4H-SiC betavoltaic power sources using tritium radioisotopes,” *Applied Physics Letters*, vol. 108, no. 1, pp. 1–5, 2016.

Chapter 5

Discussion & Conclusion

5.1 Summary & Discussion

Overall, the goal of this thesis – to determine the optimum NW BV device design – has been achieved. The top performing devices all utilize core-shell NWs that are grown as long as possible (10 μm) to accommodate the most source loading. It should be noted that longer NWs would realize improvements upon the devices reported here. Table 5.1 summarizes the performance of the top devices in terms of total efficiency, power density and energy density. Despite the lower total efficiency, devices with ^{63}Ni remain useful for long term applications due to the drastically longer half-life when compared to tritium. An additional figure of merit for energy storage devices is the specific energy (or energy per mass). This figure has been estimated by approximating the device as 1 cm^2 which is mostly made up of the Si substrate with an additional factor of safety of 1.5 (for a total device mass of 105 mg). This calculation of device mass does not account for additional components such as shielding and packaging which will need to be considered for practical device fabrication.

Table 5.1: Summary of best performing devices. All utilize core-shell NWs at a height of 10 μm .

Device	Efficiency (%)	Power Density ($\mu\text{W cm}^{-2}$)	Energy Density (Wh cm^{-2})	Specific Energy (Wh g^{-1})
GaP & ^3H	12.16	6.93	0.75	7.14
GaAs & ^{63}Ni	5.08	1.15	1.02	9.71
GaP & ^{63}Ni	5.57	1.18	1.04	9.90

Ultimately, the high performance predicted here for NW BVs is attributed to the large energy capture efficiency and minimal self-shielding, as originally predicted for this device architecture. The predicted performance of the NW BVs is competitive with top devices reported in literature. Additionally, compared to the best-case efficiency as calculated in Chapter 4, the optimized devices nearly approach their upper limit. This is especially the case for devices that utilize tritium-based sources due to the reduced self-absorption of the β particles. Therefore, the engineering of the source material in addition to structuring, is a key aspect of optimizing BV performance. Low density (low stopping power) sources are necessary to maximize energy capture efficiency and realize devices closer to the best-case predicted performance [1]. Moreover, the original heuristic of increased BV performance with increased bandgap remains valid so long as SC device losses (such as surface recombination) are minimized.

In addition to determining the optimum design, this work has also developed the first fully-coupled model for predicting the performance of NW BVs. Upon validation against experimental work, the model can continue to be expanded upon or extended to new device architectures which will be discussed below.

5.2 Future Work

First and foremost, the model presented here should be validated via experimental work. This validation would require the fabrication and testing of the optimum designs predicted here as well as intermediate designs for a more rigorous validation across a range of design variables. However, additional methods of validation/analysis can still be continued on the model presented herein. Sensitivity analysis on the model parameters should be performed to understand the effects of various practical characteristics on the overall device performance. Special attention should be placed on the effect of interaction probabilities in the Monte Carlo simulations as well as the semiconductor material properties used as parameters in the COMSOL model.

Following proper validation, the simulation tools can be expanded upon to construct a more robust and realistic model. For example, the Monte Carlo simulations can be utilized to examine the effects of thin films that accumulate at the base of the NWs as well as different passivation thicknesses [2]. Some potential improvements that can be investigated are specifically related to the drift-diffusion model in COMSOL Multiphysics. These improvements include multi-junction architectures to utilize additional energy deposited in the substrate [3] and non-homogeneous doping profiles [4] or charge-selective contacts [5], both for increased SC performance.

Beyond the future simulation work, there exist recommendations for future investigation of the BV design in general. As highlighted in Chapter 4, the engineering of the source material and chemistry is of vital importance for BV optimization. Materials engineered specifically for maximum activity loading, minimum stopping power, and practical deposition techniques are believed to be the main method for further improving performance. These source materials can be assessed via the radiation

capture simulations as GEANT4 is already equipped to simulate any arbitrary material. In addition to source deposition via spin-coating, there exists techniques such as electro- and electroless plating that have been established for printed circuit board manufacturing and would be tailored to nickel-based sources [6]. Conformal coating or plating of the NWs is of particular interest for the combination of core-shell designs with pure metal source materials as it could improve charge collection by contacting at all interfaces between the NWs and source. Overall, an understanding of source deposition and activity loading within practical devices is imperative to ensure that simulation models are able to accurately predict the device performance. That is to say that the predictions of the model established for this thesis require that deposited source composition is known with confidence. Lastly, to achieve NWs grown to suitable lengths or beyond those presented here, techniques such as hydride vapor phase epitaxy should be investigated [7].

5.3 Conclusion

NW BVs have been modelled and rigorously optimized for several common SCs and sources. In addition to the optimization, this work outlines the first fully coupled model for the assessment of NW BV devices. Therefore, by following the methods established here, future devices can be assessed before fabrication.

Monte Carlo simulations were used to investigate the radiation capture, and it was discovered that the NW array diameter and pitch can be optimized. The energy deposition profile within NWs was coupled to drift-diffusion calculations and used to predict the device output. Through various optimization techniques such as direct-search and genetic algorithms, the p-i-n junction was also optimized. Both axial and

core-shell NW structures were investigated while the latter devices are predicted to outperform the former due to the mitigation of surface recombination.

The top performance predicted by the devices simulated here are competitive with devices reported in literature which confirms the benefits of NWs for BV applications. Not only has a drastic improvement in energy capture efficiency been predicted for all devices when compared to planar BVs, but it has been determined that self-shielding does not limit the NW devices. Overall, this work has predicted that NWs are capable of impressive BV performance and should continue to be studied as long-term power sources with close-to-ideal efficiencies.

References

- [1] T. R. Alam, M. G. Spencer, M. A. Prelas, and M. A. Pierson, “Design and optimization of radioisotope sources for betavoltaic batteries,” *International Journal of Energy Research*, vol. 42, no. 7, pp. 2564–2573, 2018.
- [2] G. Otnes and M. T. Borgström, “Towards high efficiency nanowire solar cells,” *Nano Today*, vol. 12, pp. 31–45, 2017.
- [3] P. Krogstrup *et al.*, “Single-nanowire solar cells beyond the shockley–queisser limit,” *Nature Photonics*, vol. 7, no. 4, pp. 306–310, 2013.
- [4] D. Murthy *et al.*, “Efficient photogeneration of charge carriers in silicon nanowires with a radial doping gradient,” *Nanotechnology*, vol. 22, no. 31, p. 315710, 2011.
- [5] S. Z. Oener *et al.*, “Charge carrier-selective contacts for nanowire solar cells,” *Nature communications*, vol. 9, no. 1, pp. 1–7, 2018.
- [6] T. M. Gill *et al.*, “Conformal electroless nickel plating on silicon wafers, convex and concave pyramids, and ultralong nanowires,” *ACS applied materials & interfaces*, vol. 10, no. 26, pp. 22834–22840, 2018.
- [7] G. Avit *et al.*, “Ultralong and defect-free gan nanowires grown by the hvpe process,” *Nano letters*, vol. 14, no. 2, pp. 559–562, 2014.

Appendix A

Supporting Information for Ch. 3

This appendix is the published supporting information for the paper “Design and Optimization of Nanowire Betavoltaic Generators” by D.L. Wagner, D.R. Novog, and R.R. LaPierre.

Derivation of Power Captured by Nanowires

Table A.1: Variables used in radiation interaction simulations.

Variable	Symbol	Units
Power input	P_{in}	W cm^{-2}
Source volume within unit-cell	V_s	cm^3
Source Density	ρ_s	g cm^{-3}
Source specific activity	a	$\text{Ci g}^{-1} = \text{s}^{-1} \text{g}^{-1}$
Unit-cell (simulated) area	A	cm^2
Elementary charge	q	C
Energy deposited in NW	$E_{dep}(r, z)$	eV cm^{-3}
Energy capture efficiency	η_{ec}	%
Radius of NW	R	cm
Height of NW	H	cm
Energy input	E_{in}	eV
Number of histories in Monte Carlo Calculations	N	#
Average β energy of source	\bar{E}	eV
Total power captured by NWs	P_{cap}	W cm^{-2}
Nanowire areal number density	n_A	cm^{-2}

Referring to Table A.1, the power input per device square area is known for each simulation. It is given by:

$$P_{in} = q \frac{V_s \rho_s a}{A} \bar{E}. \quad (\text{A.1})$$

From GEANT4, the spatial energy deposition within a single NW, and the energy capture efficiency of both NWs within the non-primitive unit cell, are related through:

$$2\pi \int_{r=0}^R \int_{z=0}^H E_{dep}(r, z) r dz dr = \frac{\eta_{ec} E_{in}}{2} \quad (\text{A.2})$$

where $\lim_{N \rightarrow \infty} E_{in} = \bar{E}$. Note that the factor of 1/2 in Equation A.2 is used to account for all converter volumes in the simulated unit-cell. In addition, with sufficiently high

N , the total power deposited within all NWs, P_{cap} , is calculated as:

$$\begin{aligned} P_{cap} &= P_{in}\eta_{ec} \\ &= P_{in} \left(2\pi \frac{2}{E} \int_{r=0}^R \int_{z=0}^H E_{dep}(r, z) r dz dr \right) \\ &= 2\pi (qV_s \rho_s a) n_A \int_{r=0}^R \int_{z=0}^H E_{dep}(r, z) r dz dr, \end{aligned} \tag{A.3}$$

Radioisotope Spectra

The source spectra for both nickel-63 and tritium radioisotopes is shown in Figure A.1. The mean value of the β particle energy is also indicated. These are the theoretical spectra of each radioisotope and thus used as the source spectrum for all cases in GEANT4. For cases where the source material is not a pure radioisotope, the self-shielding effects automatically calculated through the Monte Carlo simulation will account for the “effective” spectrum or the spectrum observed from outside of a source material with finite volume.

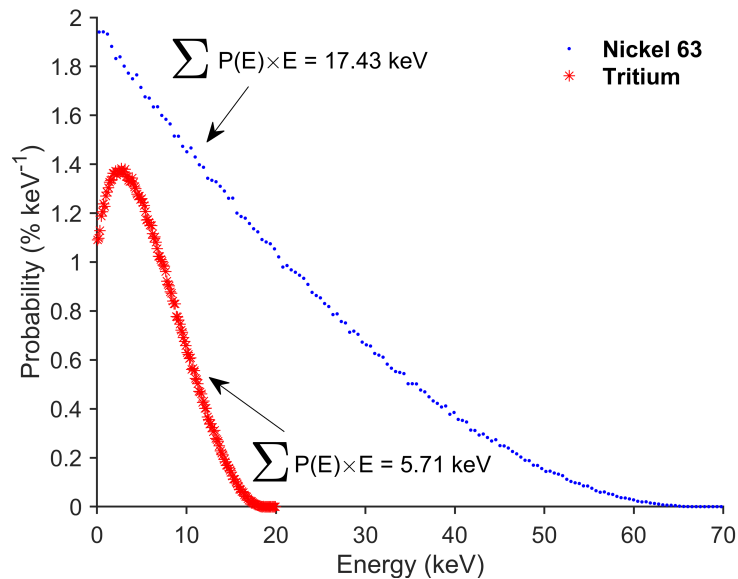


Figure A.1: β particle spectra of nickel-63 and tritium as defined in GEANT4 Monte Carlo simulations.

Optimum Nanowire Diameter Behavior

In order to investigate possible reasons for the behaviour of optimum NW diameters with increasing NW height, several fictitious source materials were simulated. The source material was modeled by varying its density and atomic composition such that the stopping power was altered relative to the NW material. Sources were also modeled with both the β spectra of nickel-63 and tritium. The results confirm that the curvature of the optimum diameter curve is independent of the β spectrum, but instead is related to the *relative* differences between the NW and radioisotope source composition. When the density (or stopping power) of the source is greater than that of the NW, we see an increasing optimum NW diameter with increasing NW height, whereas the converse is true with a source which has a density (stopping power) lower than that of the NWs. When the NW and source densities are the same, the optimum NW diameter remains constant over the range of NW lengths simulated.

This is explained physically by considering the path length of β particles within the source volume: for taller NWs and source layer, β particles will, on average, have a larger residence time within the source before interacting with a NW. Therefore, for source materials with a high stopping power compared to the NW, a larger NW diameter (converter target) is preferable over a high device activity. The converse is true for sources with a lower stopping power than the NWs: a smaller diameter (and hence a larger source volume) is not as detrimental due to minimal self-shielding in low density materials and therefore, a higher device activity is preferable.

Total Captured Power of Optimum NW Arrays

Table S2 indicates the total (integrated) captured power in the NWs and the substrate for each design combination. Using these values, the relationship between captured power and EHP generation rate as defined in Equation 3.2 and Equation 3.3, as well as the representative distribution shown in Figure 3.3, any EHP generation rate distribution can be recovered.

Table A.2: The integrated captured power in NWs and the substrate (listed in that order) for all design combinations. All quantities are given in units of nW cm^{-2} .

Nanowire Length (μm)		1.5	3	5	7.5	10
Silicon	Nickel-63	471.5	1319.9	2564.0	4173.9	5782.7
		695.3	847.1	869.7	869.8	864.0
	Nickel Citrate	45.7	136.9	282.8	482.6	691.3
		82.1	132.1	151.5	167.0	173.5
	Tritium	3575.4	9359.0	17476.5	27756.4	38096.3
		1253.2	1583.8	1723.3	1776.6	1801.0
	Tritiated Butyl	2351.0	5645.8	10072.2	15577.0	21132.8
		631.9	669.9	675.9	656.5	687.5
Gallium Arsenide	Nickel-63	714.2	1932.3	3641.8	5803.1	7953.4
		628.6	710.0	720.3	724.5	720.1
	Nickel Citrate	67.1	196.8	395.4	656.1	921.8
		75.3	104.7	119.8	125.6	127.6
	Tritium	4203.3	10550.7	19310.0	30310.0	41331.4
		1043.7	1241.9	1322.4	1359.8	1393.6
	Tritiated Butyl	2809.3	6568.9	11600.0	17879.5	24162.2
		536.6	557.1	562.7	561.0	569.3
Gallium Phosphide	Nickel-63	646.2	1762.4	3364.7	5383.9	7196.0
		657.9	771.9	782.0	770.9	745.2
	Nickel Citrate	61.1	179.8	365.5	613.1	866.3
		77.6	112.7	129.9	138.2	141.3
	Tritium	4113.3	10408.4	19107.9	30058.1	41292.8
		1083.2	1304.8	1391.9	1438.5	1502.1
	Tritiated Butyl	2744.6	6452.9	11397.4	17573.8	23577.1
		561.9	573.4	574.3	588.3	596.3

The optimum NW diameter for each design combination and the corresponding values of energy capture efficiency are shown in Figure A.2. The relative magnitude in energy capture for both tritium-based sources is as expected when compared to the total captured power. However, although nickel-63 exhibits a larger total captured power, the lower density of nickel citrate results in a higher energy capture efficiency between the two.

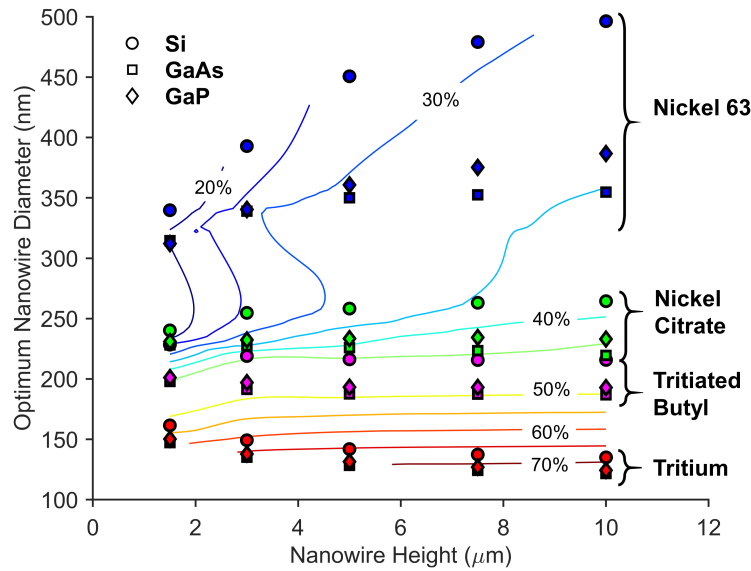


Figure A.2: Optimum nanowire diameter as a function of nanowire height for all semiconductor and radioisotope combinations. The contour lines indicate the energy capture efficiency of each optimized array design.

Comparison of Captured Power of Optimum NW Arrays to Planar Devices

Figure A.3 shows the captured power for optimized NW array geometry, P_{cap}^{NW} , using various semiconductors and radioisotope sources. NW devices were simulated across a range of NW heights from 1.5 to 10 μm . For each case, the specific activity (activity in units of Ci cm^{-2}) was calculated and set as the benchmark for equivalent planar devices, such that the source thickness was selected to match this power input. Self-shielding effects become dominant for high power inputs when using conventional planar devices, as seen by the saturating behavior of captured power for planar devices, P_{cap}^{planar} . In addition, a factor of relative improvement, calculated as:

$$\frac{P_{cap}^{NW}}{P_{cap}^{planar}} - 1 \quad (\text{A.4})$$

indicates an enhancement in energy capture efficiency of up to approximately 7, 3, 5, and 9 for nickel-63, nickel citrate, tritium, and tritiated butyl devices, respectively.

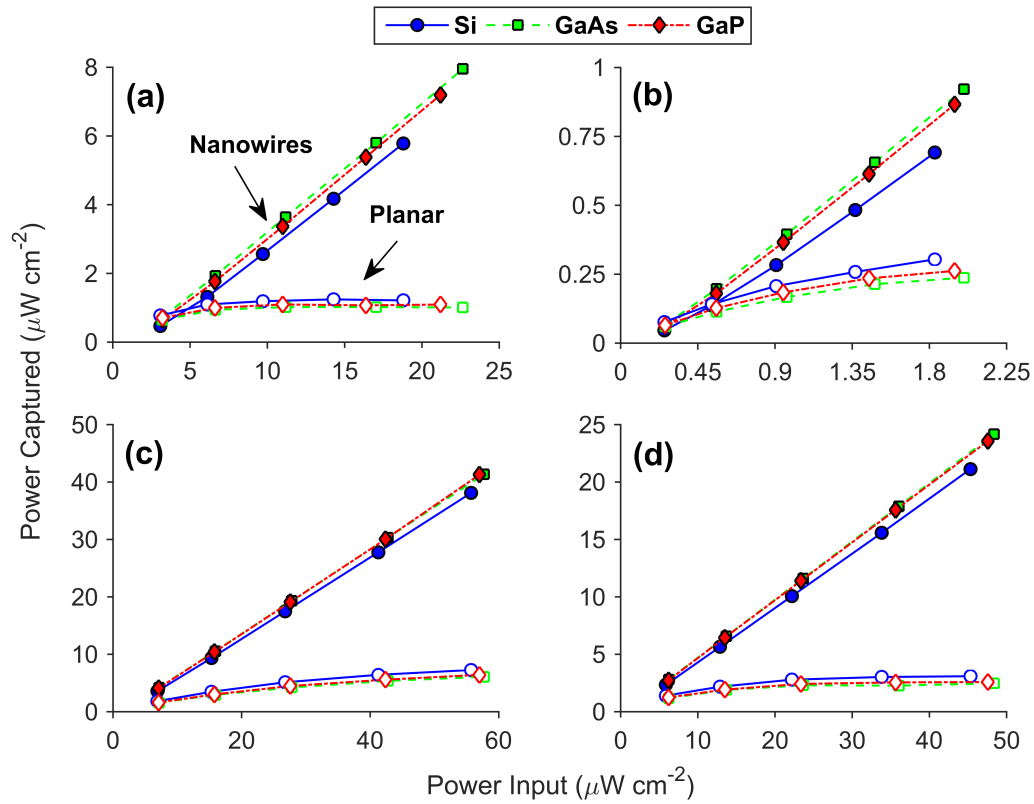


Figure A.3: Captured power for optimized nanowire devices as compared to planar devices with equivalent power inputs. The radioisotope source in each case is (a) nickel-63, (b) nickel citrate, (c) tritium, and (d) tritiated butyl.

Semiconductor Material Parameters used in COMSOL Model

Table A.3 provides the quantities required for the drift-diffusion calculations for each candidate semiconductor. Where applicable, Eq. (S5), (S6) and (S7) were used to calculate the minority carrier mobility, μ , the minority carrier diffusion length, L , and the minority carrier lifetime, τ , respectively. All of these models use various fitting parameters and depend on the net dopant concentration in cm^{-3} , N .

$$\mu(N) = \mu_a + \frac{\mu_b - \mu_a}{1 + \left(\frac{N}{N_{ref}}\right)^d} \quad (\text{A.5})$$

$$L(N) = \begin{cases} L' & N \leq N' \\ \frac{L_0}{1 + \left(\frac{N}{N_{ref}}\right)^d} & N > N' \end{cases} \quad (\text{A.6})$$

$$\tau(N) = \frac{\tau_0}{1 + \left(\frac{N}{N_{ref}}\right)^d} \quad (\text{A.7})$$

Table A.3: Semiconductor properties used in COMSOL Multiphysics simulations.

Property \ Semiconductor	Silicon ¹	Gallium Arsenide	Gallium Phosphide	
Background (impurity) concentration (cm^{-3})	1×10^{15} [1]	1×10^{15} [2]	1×10^{15} [3]	
Surface state (electron) density (cm^{-2})	1×10^{12} [4]	1×10^{12} [5]	1×10^{12} [6]	
Surface recombination velocity (cm s^{-1})	10 [7] (SiO ₂)	10^3 [8] (AlGaAs)	10^4 [9] (AlGaP)	
Radiative recombination coefficient ($\text{cm}^3 \text{s}^{-1}$)	–	1×10^{-10} [10]	1×10^{-13} [11]	
Auger recombination coefficient ($\text{cm}^6 \text{s}^{-1}$)	Electrons	2.8×10^{-31} [12]	1.5×10^{-31} [13]	1.0×10^{-30} [14]
	Holes	9.9×10^{-32} [12]	2.0×10^{-30} [13]	1.0×10^{-30} [14]

Minority electron lifetime (s)	τ_0	1.7×10^{-5} [15]	1.0×10^{-6} [16]	–
	N_{ref} (cm ⁻³)	1.7×10^{15} [15]	1.0×10^{16} [16]	–
Minority hole lifetime (s)	τ_0	3.95×10^{-4} [15]	2.00×10^{-8} [16]	–
	N_{ref} (cm ⁻³)	7.1×10^{15} [15]	2.0×10^{18} [16]	–
Minority electron diffusion length (cm)	L_0	–	–	0.0503 [17]
	N_{ref} (cm ⁻³)	–	–	3.45×10^{15} [17]
	L'	–	–	3.72×10^{-4} [17]
	N' (cm ⁻³)	–	–	1.00×10^{18} [17]
	d (–)	–	–	0.8734 [17]
Minority hole diffusion length (cm)	L_0	–	–	0.001 [17]
	N_{ref} (cm ⁻³)	–	–	6.78×10^{17} [17]
	L'	–	–	3.72×10^{-4} [17]
	N' (cm ⁻³)	–	–	1.38×10^{18} [17]
	d (–)	–	–	2.239 [17]
Minority electron mobility (cm ² V ⁻¹ s ⁻¹)	μ_a	88.0 [15]	500 [18]	2.39 [19]
	μ_b	1340 [15]	9400 [18]	155.9 [19]
	N_{ref} (cm ⁻³)	1.26×10^{17} [15]	6.00×10^{16} [18]	5.06×10^{18} [19]
	d (–)	0.880 [15]	0.394 [18]	0.740 [19]
Minority hole mobility (cm ² V ⁻¹ s ⁻¹)	μ_a	54.3 [15]	[18]	[19]
	μ_b	461.3 [15]	491.5 [18]	155.9 [19]
	N_{ref} (cm ⁻³)	2.35×10^{17} [15]	1.48×10^{17} [18]	1.33×10^{18} [19]
	d (–)	0.88 [15]	0.38 [18]	0.69 [19]

1: The dopant concentration (acceptors) of the silicon substrate is 1×10^{19} cm⁻³.

Internal Quantum Efficiency of Optimized Devices

The internal quantum efficiency (IQE) of a BV converter is given as the ratio of total β -generated current to the short-circuit current of the device. By examining this

quantity for each semiconductor across the range of NW heights simulated, the impact of surface recombination can be determined. Figure A.4 presents the calculated IQEs for optimized GaAs and GaP devices. Note that Si is omitted from this plot as the calculated IQEs for these devices were all equal to unity.

It is clear from Figure A.4 that the high surface recombination velocity of GaP greatly impacts its performance for longer NWs, limiting it as a BV converter for high activity generators. This study therefore highlights the importance of practical device limitations when examining optimum BV design; although a higher bandgap is attractive for a high open-circuit voltage, this does not consider additional material properties which could impact device performance.

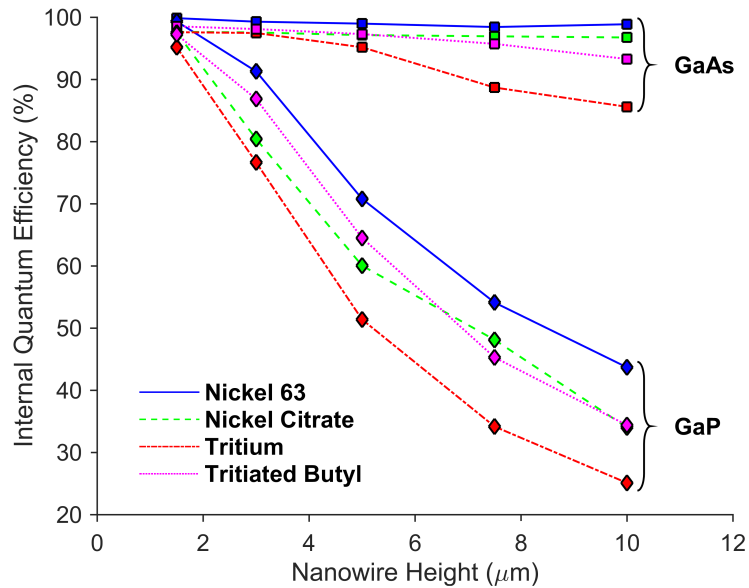


Figure A.4: Internal quantum efficiency of optimized nanowire devices. Silicon devices attained IQEs of unity for all cases and are therefore omitted.

Optimized Parameters

Table A.4 outlines the optimum parameters for each semiconductor and radioisotope combination. The corresponding performance (maximum power point and efficiency) is also indicated.

Table A.4: Summary of optimization results. For each combination of NW material, source, and NW length, the parameters are listed in order of p-type thickness (nm), n-type thickness (nm), p-type dopant concentration ($1 \times 10^{17} \text{ cm}^{-3}$), n-type dopant concentration ($1 \times 10^{17} \text{ cm}^{-3}$), maximum power point (nW cm^{-2}), and ultimate efficiency (%).

Nanowire Length (μm)		1.5	3	5	7.5	10
Silicon	Nickel-63	100	450	700	900	1250
		130	200	225	250	300
		2.00	3.25	4.00	6.50	10.00
		50.00	50.00	50.00	50.00	50.00
		43.7	114.6	216.8	378.7	483.4
		1.42	1.87	2.23	2.65	2.57
	Nickel Citrate	375	400	550	650	800
		100	175	250	325	350
		1.00	2.00	2.50	5.00	9.35
		50.00	50.00	50.00	50.00	50.00
		3.7	9.3	18.7	35.2	49.4
		1.44	1.75	2.06	2.58	2.70
Tritium	300	350	500	525	600	
	300	325	400	450	475	
	3.00	8.00	16.00	20.00	30.00	
	50.00	50.00	50.00	50.00	50.00	
	376.0	979.8	1826.0	2996.0	3851.2	
	5.46	6.39	6.82	7.26	6.92	
Tritiated Butyl	175	180	300	375	450	
	250	350	400	425	450	
	3.00	6.00	6.50	10.00	16.00	
	50.00	50.00	50.00	50.00	50.00	
	221.3	543.0	970.4	1536.9	2023.9	
	3.78	4.22	4.37	4.54	4.47	

		100	100	100	150	220
		150	300	375	400	450
	Nickel-63	100.00	100.00	100.00	100.00	100.00
		31.00	30.00	28.00	23.00	22.50
		70.5	221.7	441.0	718.5	1067.2
		2.20	3.34	3.95	4.22	4.71
		50	75	100	200	350
		150	350	500	560	600
	Nickel Citrate	100.00	100.00	100.00	100.00	100.00
		40.00	34.00	31.00	24.00	19.50
		5.3	17.2	34.6	63.8	104.7
		2.02	3.07	3.58	4.31	5.23
Gallium Arsenide		60	110	200	350	570
		125	200	275	300	310
	Tritium	100.00	100.00	100.00	100.00	100.00
		50.00	50.00	50.00	45.00	40.00
		482.5	1313.9	2526.6	3944.2	5605.4
		6.74	8.26	9.09	9.23	9.71
		55	100	125	190	240
		150	215	285	350	380
	Tritiated Butyl	100.00	100.00	100.00	100.00	100.00
		50.00	48.00	47.00	46.00	45.00
		314.9	805.6	1525.2	2393.1	3426.7
		5.03	5.88	6.45	6.64	7.08
		80	100	200	450	800
		100	300	500	550	600
	Nickel-63	100.00	100.00	100.00	100.00	100.00
		10.00	17.50	27.50	30.00	40.00
		101.1	255.0	400.6	466.4	518.0
		3.14	3.86	3.64	2.85	2.44
		100	200	350	550	825
		100	250	400	475	600
	Nickel Citrate	100.00	100.00	100.00	100.00	100.00
		20.00	25.00	30.00	40.00	50.00
		9.0	23.2	35.2	43.5	49.1
		3.47	4.16	3.71	3.00	2.52
Gallium Phosphide						

	100	300	600	1000	1600
	600	600	600	600	600
Tritium	100.00	100.00	100.00	100.00	100.00
	0.80	1.25	1.50	1.75	2.00
	671.2	1221.6	1789.0	1880.7	1890.1
	9.45	7.74	6.49	4.43	3.32
	100	150	200	400	700
	600	600	600	600	600
Tritiated Butyl	100.00	100.00	100.00	100.00	100.00
	0.70	0.95	1.00	1.00	1.00
	475.0	915.2	1299.3	1409.6	1435.2
	7.65	6.78	5.56	3.96	3.02

References

- [1] W. E. Spear and P. G. Le Comber, “Substitutional doping of amorphous silicon,” *Solid State Communications*, vol. 88, no. 11-12, pp. 1015–1018, 1993.
- [2] N. I. Goktas, E. M. Fiordaliso, and R. R. LaPierre, “Doping assessment in GaAs nanowires,” *Nanotechnology*, vol. 29, no. 23, 2018.
- [3] R. M. Biefeld, “The preparation of device quality gallium phosphide by metal organic chemical vapor deposition,” *Journal of Crystal Growth*, vol. 56, no. 2, pp. 382–388, 1982.
- [4] B. E. Deal, M. Sklar, A. S. Grove, and E. H. Snow, “Characteristics of the Surface-State Charge (Q_{ss}) of Thermally Oxidized Silicon,” *Journal of the Electrochemical Society*, vol. 114, no. 3, pp. 266–274, 1967.
- [5] S. E. Laux, D. J. Frank, and F. Stern, “Quasi-one-dimensional electron states in a split-gate GaAs/AlGaAs heterostructure,” *Surface Science*, vol. 196, no. 1-3, pp. 101–106, 1988.
- [6] W. H. Lubberhuizen, D. Vanmaekelbergh, and E. Van Faassen, “Recombination of photogenerated charge carriers in nanoporous gallium phosphide,” *Journal of Porous Materials*, vol. 7, no. 1, pp. 147–152, 2000.

- [7] T. Lauinger, J. Schmidt, A. G. Aberle, and R. Hezel, "Record low surface recombination velocities on 1 cm p-silicon using remote plasma silicon nitride passivation," *Applied Physics Letters*, vol. 68, no. 9, pp. 1232–1234, 1996.
- [8] A. K. J.M. Olson, R.K., Ahrenkiel, D.J. Dunlavy, Brian Keyes, "Ultralow recombination velocity at Ga_{0.5}In_{0.5}P/GaAs Heterointerfaces," *Applied Physics Letters*, vol. 1208, no. December 1998, pp. 10–13, 1989.
- [9] X. Lu, R. Hao, M. Diaz, R. L. Opila, and A. Barnett, "Improving GaP solar cell performance by passivating the surface using Al_xGa_{1-x}P epi-layer," *IEEE Journal of the Electron Devices Society*, vol. 1, no. 5, pp. 111–116, 2013.
- [10] Y. P. Varshni, "Band-to-Band Radiative Recombination in Groups IV, VI, and III-V Semiconductors (I)," *Physica Status Solidi (B) Basic Solid State Physics*, pp. 459–514, 1967.
- [11] A. P. Levanyuk and V. V. Osipov, "Edge Luminescence of Direct-Gap Semiconductors," *Soviet Physics - Uspekhi*, vol. 24, no. 3, pp. 187–215, 1981.
- [12] M. J. Kerr and A. Cuevas, "General parameterization of Auger recombination in crystalline silicon," *Journal of Applied Physics*, vol. 91, no. 3, pp. 2473–2480, 2002.
- [13] U. Strauss, W. W. Rühle, and K. Köhler, "Auger recombination in intrinsic GaAs," *Applied Physics Letters*, vol. 62, no. 1, pp. 55–57, 1993.
- [14] A. A. Bergh and P. J. Dean, "Light-emitting diodes," *Oxford, Clarendon Press, 1976. 598 p*, 1976.
- [15] N. D. Arora, J. R. Hauser, and D. J. Roulston, "Electron and Hole Mobilities in Silicon as a Function of Concentration and Temperature," *IEEE Transactions on Electron Devices*, vol. 29, no. 2, pp. 292–295, 1982.

- [16] M. S. Lundstrom, M. E. Klausmeier-Brown, M. R. Melloch, R. K. Ahrenkiel, and B. M. Keyes, “Device-related material properties of heavily doped gallium arsenide,” *Solid State Electronics*, vol. 33, no. 6, pp. 693–704, 1990.
- [17] M. L. Young and D. R. Wight, “Concentration dependence of the minority carrier diffusion length and lifetime in GaP,” *Journal of Physics D: Applied Physics*, vol. 7, no. 13, pp. 1824–1837, 1974.
- [18] M. Sotoodeh, A. H. Khalid, and A. A. Rezazadeh, “Empirical low-field mobility model for III-V compounds applicable in device simulation codes,” *Journal of Applied Physics*, vol. 87, no. 6, pp. 2890–2900, 2000.
- [19] Y. C. Kao and O. Eknayan, “Electron and hole carrier mobilities for liquid phase epitaxially grown GaP in the temperature range 200-550 K,” *Journal of Applied Physics*, vol. 54, no. 5, pp. 2468–2471, 1983.

Appendix B

Supporting Information for Ch. 4

This appendix is the published supporting information for the paper “Genetic Algorithm Optimization of Core-Shell Nanowire Betavoltaic Generators” by D.L. Wagner, D.R. Novog, and R.R. LaPierre.

Curve Fitting of Optimized Energy Capture in Nanowire Arrays

Independent of the semiconductor charge transport, the radiation capture of the nanowire arrays can be optimized in order to maximize the captured β power. Using the methods outlined in [1], the captured power has been optimized for nanowires up to 10 μm in height made of silicon, gallium arsenide, or gallium phosphide for sources composed of nickel-63, nickel-citrate, tritium, or tritiated butyl. By plotting the resulting energy capture efficiency, η_{ec} , as a function of nanowire height, H , a distinct inverse power law behaviour can be seen.

A subspace trust-region algorithm based on the interior-reflective Newton method is used as a nonlinear least-squares fit approach [2]. The energy capture efficiencies are fit to the form of:

$$\eta_{ec}(H) = \frac{a}{H^b} + c \quad (\text{B.8})$$

where a , b , and c , are the fit coefficients. Note that b and c are constrained to be strictly positive. Table B.1 provides the coefficients and the 95% confidence intervals for each. The adjusted R^2 values for all fits are in excess of 0.99. Figure B.1 shows the curve fitting for each semiconductor/source combination as well as the associated 95% prediction intervals.

Table B.1: Curve fit coefficients for energy capture efficiency of optimized nanowire arrays. 95% confidence intervals are given.

Semiconductor	Radioisotope	a	b	c
Silicon	^{63}Ni	-31.14 ± 9.93	0.65 ± 0.33	37.23 ± 14.03
	$^{63}\text{Ni-Cit}$	-43.90 ± 16.97	0.45 ± 0.37	52.42 ± 19.95
	^3H	-28.80 ± 1.46	0.94 ± 0.16	71.53 ± 1.30
	Trit-Butyl	-11.28 ± 0.63	1.00 ± 0.17	47.62 ± 0.48
Gallium Arsenide	^{63}Ni	-22.65 ± 0.89	0.80 ± 0.12	38.64 ± 1.06
	$^{63}\text{Ni-Cit}$	-38.58 ± 3.27	0.57 ± 0.16	56.12 ± 4.45
	^3H	-22.78 ± 1.54	1.11 ± 0.20	73.23 ± 0.91
	Trit-Butyl	-8.93 ± 0.28	1.11 ± 0.09	50.60 ± 0.16
Gallium Phosphide	^{63}Ni	-27.92 ± 2.29	0.51 ± 0.12	42.77 ± 2.98
	$^{63}\text{Ni-Cit}$	-42.86 ± 9.90	0.46 ± 0.27	58.82 ± 12.41
	^3H	-25.79 ± 1.96	0.74 ± 0.21	77.12 ± 2.57
	Trit-Butyl	-10.01 ± 0.83	1.30 ± 0.23	50.10 ± 0.33

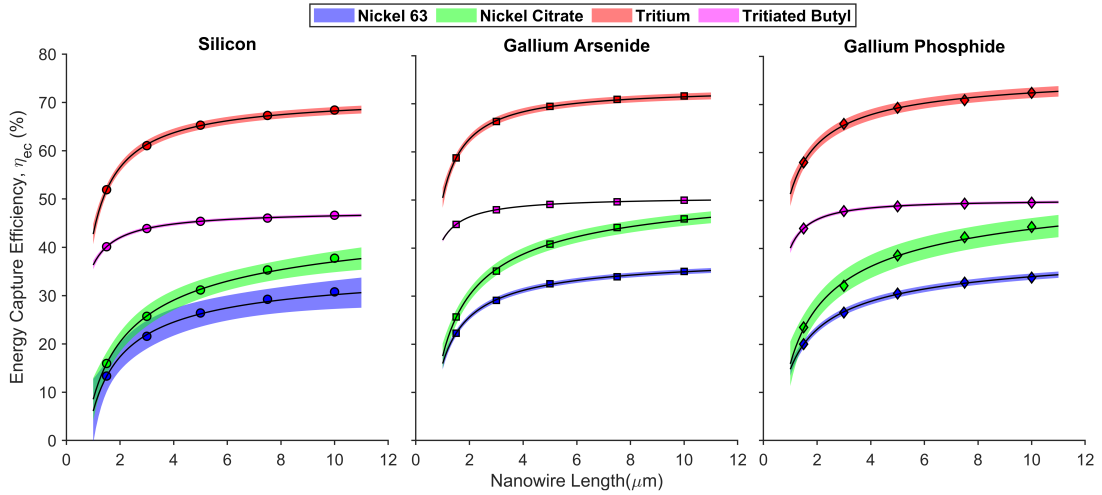


Figure B.1: Curve fits for energy capture efficiency of optimized nanowire arrays. The shaded region indicates the 95% confidence prediction interval.

Power Input of Optimum Nanowire Array Geometry

The power density input of the optimized arrays examined in this work is calculated as the product of the volume of the radioisotope between the nanowires, V , (using the optimum diameter and pitch from [3]), as well as the specific activity, ϕ , density, ρ , and average β energy of the source, \bar{E} . These source parameters are given in Table B.2. Tritium gas has been used in betavoltaic device fabrication and has been defined here at standard ambient temperature and pressure (298 K and 1 atm). The overall power density input as a function of nanowire height is given in Figure B.2. It is clear that the power is linear with nanowire length. Therefore, for the calculations of best-case device efficiency discussed below, this data can be extrapolated to determine the overall power input for the optimum design of longer nanowires.

Table B.2: Radioisotope source properties [4].

Radioisotope	ϕ (Ci g ⁻¹)	ρ (g cm ⁻³)	\bar{E} (keV)
⁶³ Ni	56.03	8.908	17.43
⁶³ Ni-Cit	18.70	1.85	17.43
³ H	9600	0.25	5.71
Trit-Butyl	1900	1.25	5.71

No correction factors are used to calculate the power input. This is feasible because the radiation capture simulations of previous work utilize a volumetric source where the stopping power of the source itself is already considered. Therefore, self-shielding is automatically accounted for in the energy capture simulations [5, 6].

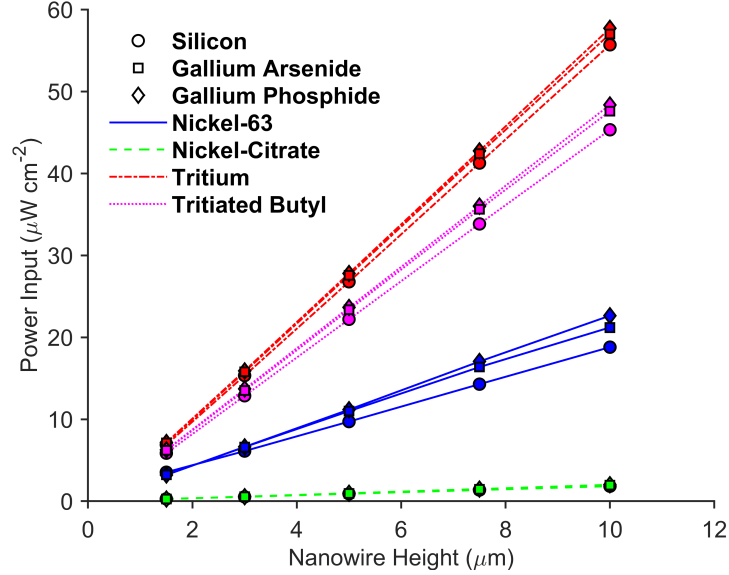


Figure B.2: The power density input for optimized nanowire arrays.

Calculation of Best-case Core-shell Nanowire Betavoltaic Efficiency

The quantities required to calculate the best-case nanowire betavoltaic efficiency as defined in the main text are provided in Table B.3.

The minimum values of the reverse saturation current density, J_0 , are achieved at the following acceptor and donor dopant concentrations (N_A and N_D , respectively):

- Silicon: $N_A = 1 \times 10^{19} \text{ cm}^{-3}$, $N_D = 5 \times 10^{18} \text{ cm}^{-3}$
- Gallium Arsenide: $N_A = 1 \times 10^{19} \text{ cm}^{-3}$, $N_D = 5 \times 10^{18} \text{ cm}^{-3}$
- Gallium Phosphide: $N_A = 1 \times 10^{19} \text{ cm}^{-3}$, $N_D = 7.7 \times 10^{17} \text{ cm}^{-3}$

Note that these dopant concentrations are those which minimize J_0 and do not necessarily maximize overall device performance. The maximum values of the short-circuit current density, J_{sc} , are calculated by solving Equation B.8 for an energy

capture efficiency of 99% the maximum value. This ensures the devices have a finite size, H . The corresponding power input, P_{in} , is extrapolated from Figure B.2 and used in:

$$J_{sc} = \frac{P_{in} \cdot \eta_{ec}}{\varepsilon} \quad (\text{B.9})$$

where the values of the ionization energy, ε , for silicon, gallium arsenide, and gallium phosphide are (3.8 ± 0.01) , (4.6 ± 0.06) , and (7.8 ± 0.8) eV, respectively [7, 8].

Table B.3: Intermediate results of best-case nanowire device efficiency calculation. The uncertainty on V_{oc} arises due to the confidence bounds on the ideal energy capture efficiency, and thus J_{sc} .

Semiconductor	Radioisotope	J_0 (A cm ⁻²)	H (μm)	J_{sc} (A cm ⁻²)	V_{oc} (mV)
Silicon	⁶³ Ni	2.56×10^{-14}	954.9	1.68×10^{-4}	587.8 ± 38.8
	⁶³ Ni-Cit		1706.5	4.30×10^{-5}	552.3 ± 24.9
	³ H		51.1	5.49×10^{-5}	558.6 ± 1.4
	Trit-Butyl		23.4	1.35×10^{-5}	522.1 ± 1.0
Gallium Arsenide	⁶³ Ni	1.74×10^{-20}	159.4	3.07×10^{-5}	912.7 ± 4.1
	⁶³ Ni-Cit		1569.7	3.92×10^{-5}	919.1 ± 7.6
	³ H		22.2	2.07×10^{-5}	902.4 ± 0.7
	Trit-Butyl		13.2	7.09×10^{-6}	874.6 ± 1.0
Gallium Phosphide	⁶³ Ni	3.10×10^{-33}	3644.0	4.24×10^{-4}	1744.3 ± 13.7
	⁶³ Ni-Cit		10711.0	1.60×10^{-4}	1719.0 ± 29.9
	³ H		115.6	6.70×10^{-5}	1696.3 ± 3.2
	Trit-Butyl		10.0	3.07×10^{-6}	1616.2 ± 1.7

References

- [1] D. Wagner, D. R. Novog, and R. R. LaPierre, “Simulation and optimization of current generation in gallium phosphide nanowire betavoltaic devices,” *Journal of Applied Physics*, vol. 125, no. 16, 2019.
- [2] T. F. Coleman and Y. Li, “An interior trust region approach for nonlinear minimization subject to bounds,” *SIAM Journal on optimization*, vol. 6, no. 2, pp. 418–445, 1996.
- [3] D. Wagner, D. R. Novog, and R. R. LaPierre, “Design and Optimization of Nanowire Betavoltaic Generators,” *Journal of Applied Physics*, vol. 128, no. 1, 2020.
- [4] S. Agostinelli *et al.*, “GEANT4 – a simulation toolkit,” *Nuclear Instruments and Methods in Physics Research Section A: Accelerators, Spectrometers, Detectors and Associated Equipment*, vol. 506, no. 3, pp. 250–303, 2003.
- [5] C. Thomas, S. Portnoff, and M. G. Spencer, “High efficiency 4H-SiC betavoltaic power sources using tritium radioisotopes,” *Applied Physics Letters*, vol. 108, no. 1, pp. 1–5, 2016.
- [6] G. Gui, K. Zhang, J. P. Blanchard, and Z. Ma, “Prediction of 4H-SiC betavoltaic microbattery characteristics based on practical Ni-63 sources,” *Applied Radiation and Isotopes*, vol. 107, pp. 272–277, 2016.

- [7] C. A. Klein, “Bandgap dependence and related features of radiation ionization energies in semiconductors,” *Journal of Applied Physics*, vol. 39, no. 4, pp. 2029–2038, 1968.
- [8] G. Bertuccio and D. Maiocchi, “Electron-hole pair generation energy in gallium arsenide by x and γ photons,” *Journal of Applied Physics*, vol. 92, no. 3, pp. 1248–1255, 2002.